AFRL-VS-TR-2002-1666

# APPLICATION OF RADIATIVE TRANSFER TECHNIQUES TO BACKGROUND CLUTTER MITIGATION

Peter P. Wintersteiner

ARCON Corporation
260 Bear Hill Road
Waltham, MA 02451-1080

22 October 2002

Final Report






AIR FORCE RESEARCH LABORATORY
Space Vehicles Directorate
29 Randolph Rd
AIR FORCE MATERIEL COMMAND
Hanscom AFB, MA 01731-3010

This technical report has been reviewed and is approved for publication.

Contract Manager

Branch Chief

This document has been reviewed by the ESC Public Affairs Office and has been approved for release to the National Technical Information Service (NTIS).

Qualified requestors may obtain additional copies from the Defense Technical Information Center (DTIC). All others should apply to the NTIS.

If your address has changed, if you with to be removed from the mailing list, or if the addressee is no longer employed by your organization, please notify AFRL/VSIM, 29 Randolph Rd., Hanscom AFB, MA 01731-3010. This will assist us in maintaining a current mailing list.

Do not return copies of this report unless contractual obligations or notices on a specific document require that it be returned.

# REPORT DOCUMENTATION PAGE

**Form Approved**
**OMB NO. 0704-0188**



| 1. AGENCY USE ONLY ( Leave Blank) | 2. REPORT DATE | 3. REPORT TYPE AND DATES COVERED |
|---|---|---|
| | 22 October 2002 | Final Report<br>20 July 2000 to 24 July 2002 |

**4. TITLE AND SUBTITLE**
Application of Radiative Transfer Techniques to Background Clutter Mitigation

**5. FUNDING NUMBERS**
**Contract F19628-00-C-0072**
**PE 612305**
**PR 2305**
**TA BD**
**WU AA**

**6. AUTHOR(S)**
Peter P. Wintersteiner

**7. PERFORMING ORGANIZATION NAME(S) AND ADDRESS(ES)**
ARCON Corporation
260 Bear Hill Rd.
Waltham, MA, 02451-1080

**8. PERFORMING ORGANIZATION REPORT NUMBER**

**9. SPONSORING / MONITORING AGENCY (S) NAME AND ADDRESS(ES)**
Air Force Research Laboratory/VSSS
Hanscom AFB, MA 01731-3010
Contract manager: Jeremy Winick

**10. SPONSORING / MONITORING AGENCY REPORT NUMBER**
**AFRL-VS-TR-2002-1666**

**11. SUPPLEMENTARY NOTES**

**12 a. DISTRIBUTION / AVAILABILITY STATEMENT**
Approved for public release; distribution unlimited

**12 b. DISTRIBUTION CODE**

**13. ABSTRACT (Maximum 200 words)**
Radiative-transfer techniques have been applied to several problems of interest to the defense and remote-sensing communities. We looked at MWIR radiance in the presence of gravity waves. We simulated radiance structures that had been seen by the MSX satellite, and estimated the expected non-LTE contribution. We also report on our first look at some of the SABER data from the TIMED satellite.

**14. SUBJECT TERMS**
Radiative transfer; Atmospheric radiance structure; Clutter; Visible, NIR & infrared; $CO_2$ 15 μm & 4.3 μm emission; Non-LTE; ARC; SABER

**15. NUMBER OF PAGES**
39

**16. PRICE CODE**

| 17. SECURITY CLASSIFICATION OF REPORT | 18. SECURITY CLASSIFICATION OF THIS PAGE | 19. SECURITY CLASSIFICATION OF ABSTRACT | 20. LIMITATION OF ABSTRACT |
|---|---|---|---|
| Unclassified | Unclassified | Unclassified | UNL |

# Table of Contents

# List of Figures

## Preface

ARCON Corporation is pleased to submit our finished Final Report, which describes research that has been carried out under the provisions of contract F19628-00-C-0072. The period of performance for this contract was from July 20, 2000 until July 24, 2002. The overall purpose of the work that we have undertaken is to apply radiative transfer techniques, in new ways, to important problems relating to background clutter mitigation. In particular, we simulated the radiant signature of gravity waves in the MWIR and used our experience with non-LTE processes to investigate their likely contributions to the observations. We also examined SABER limb sounding data, looking at the range of radiance variability encountered.

In the process of working with the SABER team, we developed two new codes to enhance the capabilities of our non-LTE model, Atmospheric Radiance Code (ARC). These are briefly described in Section 2.

The stated purpose of investigating background clutter is well served by the work reported below. It is supplemented by the transition of some of our modeling and simulation capabilities to the Air Force, in the form of codes that we have developed for the purpose of carrying out the work outlined above, and advice or assistance related to their use. Up-to-date source code for these applications has been submitted to the Air Force on a ZIP disk. The contents of the disk are outlined in Appendix A.

# 1. Background Clutter in non-LTE Regions of the Atmosphere

Variability in atmospheric infrared radiance occurs on all spatial and temporal scales. On the largest scales, seasonal changes occur within broad latitudinal regions. On a somewhat smaller scale, diurnal effects and planetary waves modulate the emissions in ways that are at least somewhat predictable. At the same time even smaller vertical and horizontal structures are often superposed on the mean state, producing pressure/temperature perturbations and other localized effects that result in substantial changes in the emissions and the radiance levels observed by satellite-borne remote-sensing instruments. Examples of such structures are persistent temperature inversion layers in the mesosphere, gravity waves, and transient frontal disturbances. In addition, there are bright local phenomena that have little to do with the underlying atmospheric structure, the most familiar example being the aurora.

The radiant signatures of these smaller-scale phenomena offer a wealth of information about basic processes affecting the atmosphere, and are often studied for exactly that reason. At the same time, they present an obstacle to certain information-gathering tasks that are becoming more routine each year, because of the unpredictable background that they present. Therefore, the need for understanding the underlying physics at a very detailed level is complemented by a requirement to quantify the range and magnitude of radiance perturbations on a global scale.

We have taken both the physical and phenomenological approaches to studying atmospheric radiance structure. In particular, we have modeled gravity waves in the stratosphere and mesosphere in an attempt to quantify radiance effects that may be seen by downlooking satellite sensors operating in the MWIR. We also started a project to assess global radiance variability by examining data from the SABER instrument on the TIMED satellite. These efforts are described in the following two sections.

## 1.1 Modeling Gravity Wave Signatures

The study of gravity waves was conducted in order to simulate MWIR radiance structures that had been observed by the MSX satellite [*Dewan et al, 1998*] and explained in a preliminary fashion by Picard et al [*1998*]. The data were from MSX radiometer band B, which measured $CO_2$ 4.3 μm emissions in two slightly different but overlapping spectral ranges. The results of our recent study have been presented by Winick et al [*2001*] and by Picard et al [*2002*].

The short summary of the results can be stated as follows. Detailed line-by-line calculations in the MWIR for downlooking (BTH, or below the horizon) lines of sight do reproduce radiance structures much like those seen by MSX. The BTH radiance response to gravity waves in the 4.3 μm band is largely determined by the kinetic temperature profile, insofar as most of the emission seen by broadband sensors originates in the upper stratosphere where LTE prevails. However, a non-LTE contribution in daytime from waves in the upper mesosphere cannot always be ignored, at least for high Sun conditions. We also showed that a sensor's ability to discern wave structure is very sensitive to the orientation of the line-of-sight (LOS) with respect to the direction of propagation of the wave.

The detailed LOS calculations were performed using FASE, a line-by-line (LBL) code incorporating all the line overlap and continuum effects needed for looking deep into the

atmosphere. (FASE is based on the AFRL standard, FASCODE [*Clough et al, 1986*].) The viewing geometry was chosen to mimic the BTH measurements with which wave structure had been seen, namely those looking near the horizon but still below it at nadir angles of approximately 57 degrees. The MSX B1 spectral filter function [*Gardiner et al, 1994*] was used in these calculations.

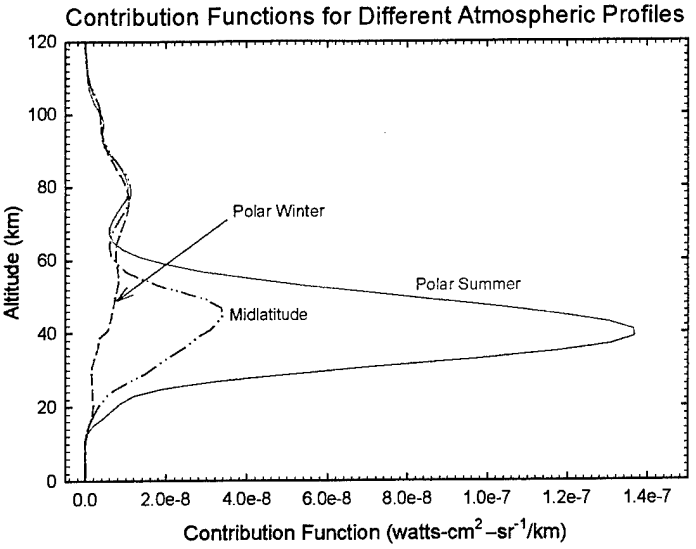


Figure 1. MSX B1-band contribution functions for three different model atmospheres.

FASE was also used to generate contribution functions (CFs). These are quantities that record the absolute inband radiance contributions reaching a detector from within each layer along a particular LOS. As such, they are sensitive to the source function at each point along the LOS and the optical path through each layer, and their sum over layers equals the total LOS radiance. They immediately show the distribution of altitudes within which the detected emissions arise. This is how the observations were associated with upper-stratospheric thermal structure [*Picard et al, 1998*].

Figure 1 gives examples of CFs for three model atmospheres representing average midlatitude conditions, and polar summer and winter. The differences between the curves are largely due to different stratopause temperatures; the total radiance is much greater for the summer polar case than for the others because of this. The calculations were done for comparison purposes, assuming non-LTE conditions, a nadir angle of 57 degrees, and a solar zenith angle of 60 degrees (even for polar winter).

### 1.1.1 Rapid Calculations using Contribution Functions

Contribution functions are also useful because they enable us to simulate radiance structure in a wave-perturbed atmosphere without repeating the tedious LBL LOS calculations dozens or hundreds of times, as would otherwise be necessary for constructing an image. The following discussion outlines the procedure for doing these rapid calculations.

It is easy to show that, for a LOS divided into $N$ homogeneous layers, the monochromatic spectral radiance is given at the detector as the following sum of *spectral* contribution functions $W_{vi}$ [*Wintersteiner and Sharma, 1985*]:

$$I_v(s) = \sum_{i=1}^{N} R_{vi} e^{-\tau_{vi}} \left[1 - e^{-\Delta\tau_{vi}}\right] = \sum_{i=1}^{N} W_{vi}, \qquad (1)$$

where $R_{vi}$ is the source function in the $i^{th}$ layer, $\tau_{vi}$ is the optical path from the near side of that layer to the observer, and $\Delta\tau_{vi}$ is the optical path within the $i^{th}$ layer. The spectral contribution functions can be integrated over any given spectral range $\Delta\nu$, with a filter function $f_v$ if necessary, to get the total inband radiance as a sum of layer contributions, $W_{\Delta\nu,i}$:

$$I_{\Delta\nu}(s) = \int_{\Delta\nu} I_\nu(s) f_\nu d\nu = \sum_{i=1}^{N} W_{\Delta\nu,i}. \tag{2}$$

For LTE conditions the source function, $R_{\nu i}$, is the blackbody function. As a result, the dominant term in $W_{\Delta\nu,i}$ is nearly proportional to $\exp(-c_2\bar{\nu}/T_i)$, ignoring the very small stimulated-emission factor. Here, $c_2$ is the second radiation constant, $T_i$ is the $i^{\text{th}}$ layer temperature, and $\bar{\nu}$ is a representative energy, which we have taken to be the band center at 2349.14 $cm^{-1}$.

To perform rapid calculations, it is necessary to (1) generate CFs, $W_{\Delta\nu,i}$, numerically using an unperturbed or "background" model atmosphere. FASE does this by building the total radiance from the ground up at each layer boundary and then subtracting the results for consecutive boundaries, one by one. [Note that it is useful to have CFs for more than one nadir angle because this quantity varies along one dimension of any image; we did calculations for 56.5, 57, and 57.5 degrees.] Then (2) one determines the wave-induced change in temperature and pressure with respect to this background at those points where a LOS intersects each layer boundary. Next (3) one calculates the mean source function within each layer for the perturbed conditions, and the ratio of this quantity to the unperturbed source function. The key step is (4) to multiply each layer's CF by this ratio and sum over layers to produce the perturbed radiance. Finally, (5) one repeats steps 2-4 for a sufficient number of LOS to reveal the radiance structure. For a single LOS, the perturbed radiance so calculated is given by

$$\tilde{I}_\nu(s) = \sum_{i=1}^{N} \tilde{W}_{\Delta\nu,i} = \sum_{i=1}^{N} W_{\Delta\nu,i} e^{-c_2\bar{\nu}/\tilde{T}_i} e^{+c_2\bar{\nu}/T_i} \tag{3}$$

where $\tilde{T}_i$ is the updated layer temperature reflecting the perturbation induced by the wave.

Leaving aside the details of step (2) for the moment, some discussion of validation tests we did is called for. We ran our tests with a hydrostatically-consistent midlatitude model atmosphere that is similar to the U.S. Standard Atmosphere, but, to provide a more realistic temperature profile, lacks the original discontinuities in the thermal gradient. For a nadir viewing angle of 57 degrees, the simulated signal in the MSX B1 band from the full LBL calculation is $7.769x10^{-7}$ watt/$cm^2$-sr. The first test was to redo the calculation using the contribution functions, assuming no atmospheric perturbation. We got a result differing from the benchmark by 0.026% (two parts in the fourth significant figure). This is quite small compared to the observed radiance structure amplitude, which is about 3%.

In principle, of course, in the absence of the wave the second calculation should produce a result identical to the benchmark. Possible sources of the small error we did obtain include the choices of $\tilde{T}_i$ and $\bar{\nu}$, and numerical roundoff in the layer-by-layer subtraction that yields the CFs in the first place. We took the layer temperature $\tilde{T}_i$ to be the average of the two layer-boundary temperatures whereas the FASE algorithm chooses a Curtis-Godson weighted mean temperature for $T_i$. With the 1-km layers specified in our calculation, $\tilde{T}_i - T_i$ should be very small. However, differences of even a hundredth of a degree could cause a discrepancy of ~0.026% if they were of the same sign for most or all of the

strongly-contributing layers, so it is possible that revising the mean source function would reconcile the two calculations. Use of the mean band energy could also skew the result. A radiance-weighted average over the filter function might have been a better choice for $\bar{\nu}$, but it is not obvious that any mean value would lead to the exact result. We did not estimate the likely error due to either the choice of $\bar{\nu}$ or to roundoff. Since the numerical error is two orders of magnitude smaller than the radiance structure, we proceeded without implementing further corrections.

We also compared direct LBL calculations of the wave-perturbed radiance with the CF-generated approximation based on the background atmosphere, for various phases of the wave. These tests were done assuming a wave with a vertical wavelength of 10 km and a horizontal wavelength of 32.5 km, choices that were made to maximize the observable contrast for viewing at the nadir angle of 57 degrees. The lower-boundary forcing (see below) was such that the simulated radiance structure amplitude was about $0.26x10^{-7}$ watt/(cm$^2$-sr), or 3.3% of the mean, which is comparable to the MSX observations. Comparisons between the LBL calculations and the CF approximation revealed differences between $0.006x10^{-7}$ and $0.015x10^{-7}$ watt/(cm$^2$-sr), at worst less than 6% of the amplitude or 3% of the peak-to-trough radiance contrast. Thus, the CF algorithm gives quite a successful approximation to the full LBL result despite the simple approach it embodies. It is worth noting that only the change in atmospheric temperature and not the change in density are accounted for in these simulations, whereas FASE accounts accurately for the full effects of the modeled wave structure.

### 1.1.2 Wave Model

Lacking a generalized gravity-wave propagation model, we adopted a simple algorithm to calculate the perturbations in temperature and pressure that would accompany a wave propagating through the background atmosphere, and then developed a code called GEN_WAVES to implement it. The wave model is an idealization that assumes a plane wave of known vertical and horizontal wavelengths propagates in a fixed direction with respect to the LOS. It includes an arbitrary forcing at the lower boundary, $z_o$, and assumes that the amplitude of the temperature perturbation, which is given by $\Delta T(z)$ at any altitude $z$ higher than $z_o$, increases with altitude as $\sqrt{N(z_o)/N(z)}$. $N$ is the total number density in the background atmosphere. The amplitude of the density perturbation is then determined from the low-frequency approximation given by Walterscheid et al [*1987*]:

$$\Delta N(z) = N(z)\left[1-\frac{\Delta T(z)}{T(z)}\right] \tag{4}$$

The actual temperature and density perturbations at any point are calculated as sinusoidal functions (as shown below) of the vertical and horizontal wavelengths and the distances $(x, z)$ from the origin. A phase can be specified in order to fix the conditions at the origin, and the forcing is adjusted so as to give plausible temperature perturbations at the stratopause. It was necessary to artificially restrict the wave amplitude at high altitudes to avoid large and unrealistic temperature/density swings. This was generally done beginning at about 80 or 85 km.

One important function of the code we wrote is to determine the perturbed atmospheric state vector at the intersections of the spherical-shell layer boundaries and the LOS, be-

cause this is what is needed to specify the model atmosphere for FASE or for the approximate calculation using the CFs. It is an exercise in plane geometry to determine the horizontal distances from the origin to these intersections. In the schematic drawing of Figure 2, the origin is chosen to be the point of intersection of the LOS with the Earth's surface. Measured from that point, the horizontal distance $x_n$ at the $n^{th}$ layer boundary (at altitude $z_n$) is

$$x_n = \beta_n (R_E + z_n). \tag{5}$$

In Eq.(5), $R_E$ is the radius of the Earth and $\beta_n$ is given by

$$\beta_n = \arcsin\left(\frac{\sin\gamma_o}{\sin\gamma_m}\right) - \arcsin\left(\frac{R_E}{R_E + z_n}\frac{\sin\gamma_o}{\sin\gamma_m}\right) \tag{6}$$

where $\gamma_o$ is the nadir viewing angle and $\gamma_m$ is the nadir angle for viewing the horizon, e.g.

$$\gamma_m = \arcsin\left(\frac{R_E}{R_E + H_S}\right), \tag{7}$$

$H_S$ being the altitude of the satellite.

Although not indicated in Figure 2, we also consider lines of sight corresponding to a range of nadir angles, $\gamma$. With the origin still defined by the intersection with the ground of a LOS having a nadir angle $\gamma_o$, Eq.(5) still applies, but the generalization of Eq.(6) is

$$\beta_n = \arcsin\left(\frac{\sin\gamma_o}{\sin\gamma_m}\right) - \arcsin\left(\frac{R_E}{R_E + z_n}\frac{\sin\gamma}{\sin\gamma_m}\right) + \gamma - \gamma_o. \tag{8}$$

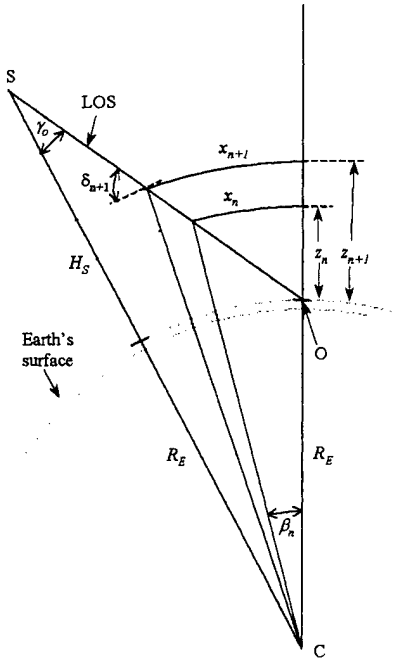


From this one can calculate the wave field at any point $(x_n, z_n)$ on the LOS, given the wavelengths and phase. That is, from the altitude-dependent temperature and density perturbation amplitudes $\Delta T(z_n)$ and $\Delta N(z_n)$, and the assumed functional form, one can easily derive the changes in temperature and density and hence the complete atmospheric state at the relevant locations. It is true that neither the geometry nor the wave model are general enough to simulate all cases of interest, but the purpose of investigating the origins of observable MWIR radiance structure is served nonetheless.

Figure 2. Schematic showing simplified geometry for BTH viewing at a nadir angle of $\gamma_o$ from a satellite S. Horizontal and vertical coordinates, with respect to the origin at O, of the intersection of the LOS with the boundaries of the $n^{th}$ atmospheric layer are indicated, as is the angle $\delta$ between the LOS and the local horizontal at the top of the layer.

### 1.1.3 Orientation of the LOS

Due the confluence of weak and strong lines, contribution functions calculated for wide spectral intervals display a broad altitude distribution. CFs shown in Figure 1 cover more than 20 km at half-maximum, which is considerably greater than typical gravity-wave vertical wavelengths. As a result, the likelihood of observing radiance structure due to waves depends on the viewing geometry. When the view intersects many wave peaks and troughs in the vicinity of the CF's maximum, cancellation occurs. Then the radiance is not much different from that of the unperturbed atmosphere and the contrast between lines of sight with slightly different viewing directions (due, for example, to slightly different nadir angles) is minimized. On the other hand, LOS with just the right orientation with respect to the wave-propagation direction may intersect only peaks or only troughs over much of the total range. In effect, each LOS sees only a single phase of the upwelling wave at all altitudes, but the phase that is seen is different for slightly different viewing angles. This is the condition that maximizes the contrast between different LOS and reveals the underlying property of the atmosphere, namely the temperature excursions that signify the passage of a wave.

For a monochromatic wave of the sort we are considering in our simple model, the propagation direction is determined by the ratio of the horizontal and vertical wavelengths, $\lambda_x$ and $\lambda_z$. Moreover, the spatial dependence of the perturbation is given by

$$\Delta T \sim \sin\left(\pm\frac{2\pi x}{\lambda_x}+\frac{2\pi z}{\lambda_z}+\phi\right) \tag{9}$$

where $\phi$ is an arbitrary phase and the choice of sign in the argument determines whether the wave is propagating toward or away from the observer. For the phase of the wave to remain constant over a range $(\Delta x, \Delta z)$ on the locus of points $(x, z)$ comprising the LOS, one can only choose waves propagating toward the observer, e.g. using the negative sign in Eq.(9). Then the condition to be satisfied is

$$\frac{\lambda_x}{\lambda_z} \approx \frac{\Delta x}{\Delta z} = \mathrm{cotan}(\delta), \tag{10}$$

where $\delta$ is the angle between the LOS and the local horizontal indicated in Figure 2. For the MSX geometry, $\delta$ is about 18.2 degrees at 40 km and the wavelength ratio is about 3.2. This relation is exact only in the limit of small $\Delta z$, since $\delta$ varies slowly with z due to the Earth's curvature. But one can also show, by the tedious exercise of expressing $x$ in terms of $z$ using Eqs.(5) and (6) and equating the phases at different altitudes, that the expression is in error by a very small amount for values of $\Delta z$ close to the width of the CFs.

A simple comparison is useful for illustrating the effect of the viewing direction. Figure 3 plots the temperature $T$ and the perturbation $\Delta T$ on the LOS near the stratopause, considering an optimally-propagating wave as specified by Eq.(10) for the MSX geometry and also a wave with the same properties but propagating in the opposite direction. In one case the temperature on the LOS is elevated with respect to the background temperature at all altitudes in the range shown. For slightly different nadir angles it would be less elevated, or diminished, at all altitudes. For the case with the wave propagating away

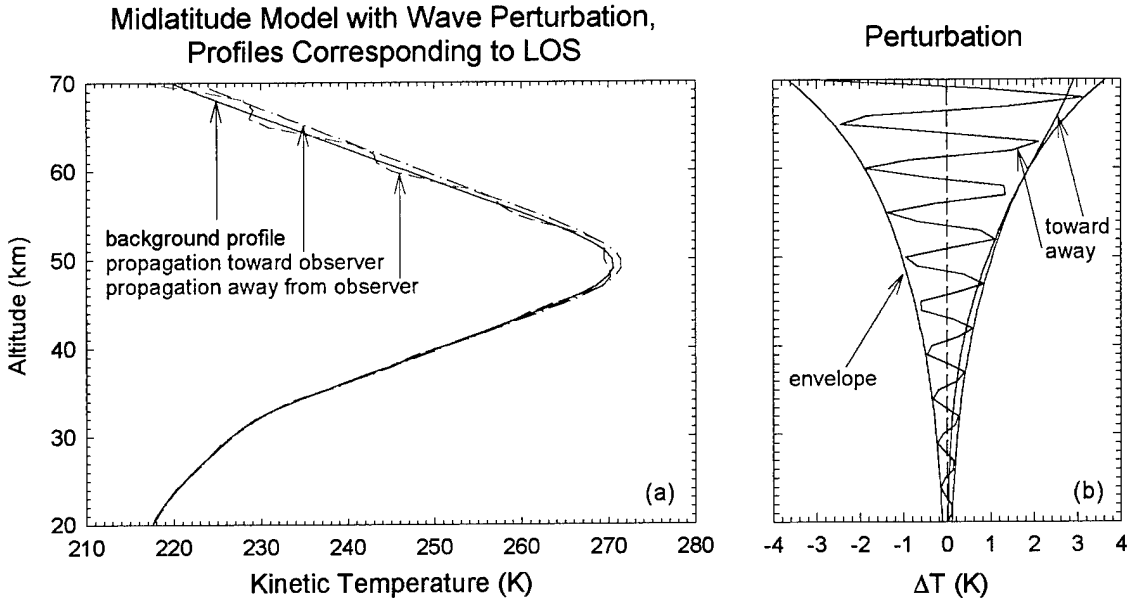


Figure 3 (a) Temperature profiles along the line of sight, for the midlatitude background model and two simulated waves propagating toward and away from the observer. The calculations were done for a nadir viewing angle of 57 degrees, assuming vertical and horizontal wavelengths of 10 and 32 km respectively so that the phase fronts of one of the waves would be nearly aligned with the LOS. (b) The perturbation with respect to the background, to illustrate that the temperature is uniformly enhanced on the LOS for the aligned case and not for the nonaligned case. See the discussion in the text.

from the observer, however, the view encounters many peaks and valleys. Here the radiance is hardly different from that of the background atmosphere, and slightly different viewing angles merely shift the altitudes on the LOS at which the peaks appear without appreciably changing the sum of the contributions from different segments of the LOS.

It follows that the viewing geometry is a critical consideration for detecting stratospheric waves through their radiant signatures. Winick et al [*2001*] calculated the radiance as a function of nadir angle for the nearly-aligned case depicted in Figure 3 and for other cases with different wavelength ratios. Figure 4, from their presentation, shows the radiance contrast for the nearly-aligned case, $\lambda_x = 32.5$ km, $\lambda_z = 10$ km on the left. The

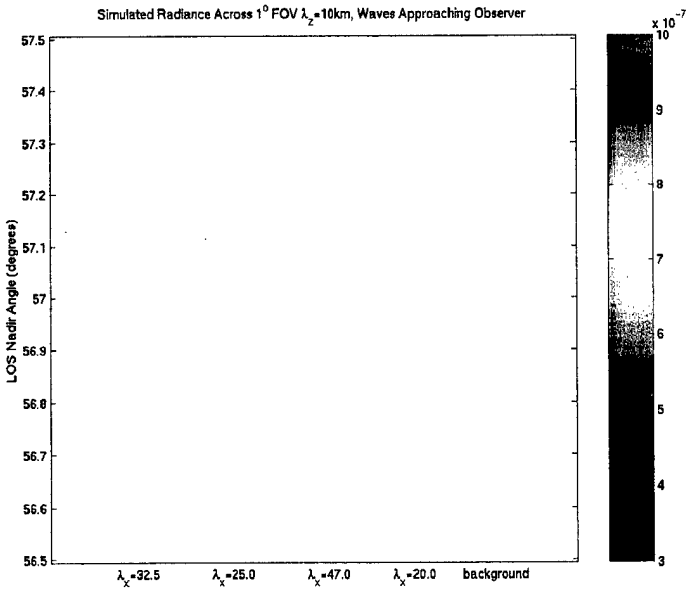


Figure 4. Simulated radiance for a 1-degree range of nadir viewing angles centered on 57 degrees, assuming different horizontal wavelengths and therefore different degrees of alignment of the phase fronts with the LOS.

cases with $\lambda_x$ equal to 25 and 47 km (everything else remaining as before) correspond to waves propagating only about 5 degrees from the "optimal" direction, but even so the contrast is much reduced. For $\lambda_x = 20$ km the discrepancy is about 10 degrees, and one can see that that radiance pattern is almost the same as that of the background atmosphere, given on the right. [The change in the viewing angle alone causes the variation within the rightmost profile in Figure 4. There is a slightly greater airmass on the LOS for larger nadir angles, resulting in greater opacity and therefore CFs that peak at slightly higher (and warmer) altitudes in the stratosphere.]

One can conclude that the viewing geometry imposes strict conditions on what can be detected and what can't. Therefore, even if upward-propagating waves are ubiquitous in the atmosphere, the probability of observing them is much reduced by geometrical/observational constraints.

### 1.1.4. Non-LTE Effects

The discussion of contribution functions, and in particular their use for rapidly determining LOS radiance in a wave-perturbed atmosphere, omitted any mention of non-LTE effects. The relevant $CO_2$ 4.3 μm states are in fact in LTE throughout the stratosphere, where the CF peaks occur, but in the mesosphere their vibrational temperatures depart from equilibrium because of radiative transfer from the warm stratopause and because of the absorption of solar flux. As a result, the total observed radiance for BTH views does include some contribution from non-LTE regions, although at night it is very small.

The non-LTE influence can be seen in the CF plots of Figure 1, where the secondary peak near 80 km is caused by greatly-elevated daytime vibrational populations. (In fact, for the polar winter model the non-LTE contribution appears dominant, which would be the actual situation if daytime conditions could actually prevail.) It is further emphasized in Figure 5, where CFs calculated for both LTE and non-LTE conditions are compared for the midlatitude model we use. The non-LTE calculations assume that the minor-isotope $CO_2$ vibrational temperatures are the same as the major-isotope temperature, a limitation of FASE that introduces a small error. But the fact that there is a significant non-LTE component to the total is apparent.

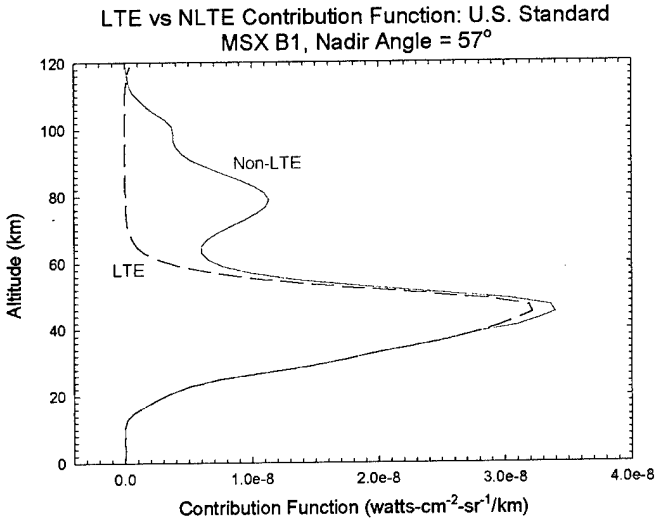


Figure 5. LTE and non-LTE contribution functions for the midlatitude model atmosphere, from FASE.

The implications that non-LTE effects have for observations of wave structure are not thoroughly understood at this time. It is important to note, however, that the kinetic and vibrational temperatures are largely decoupled above about 60 km, because the dominant excitation mechanisms for the principal emitting states are not thermal as they are at lower altitudes. As a

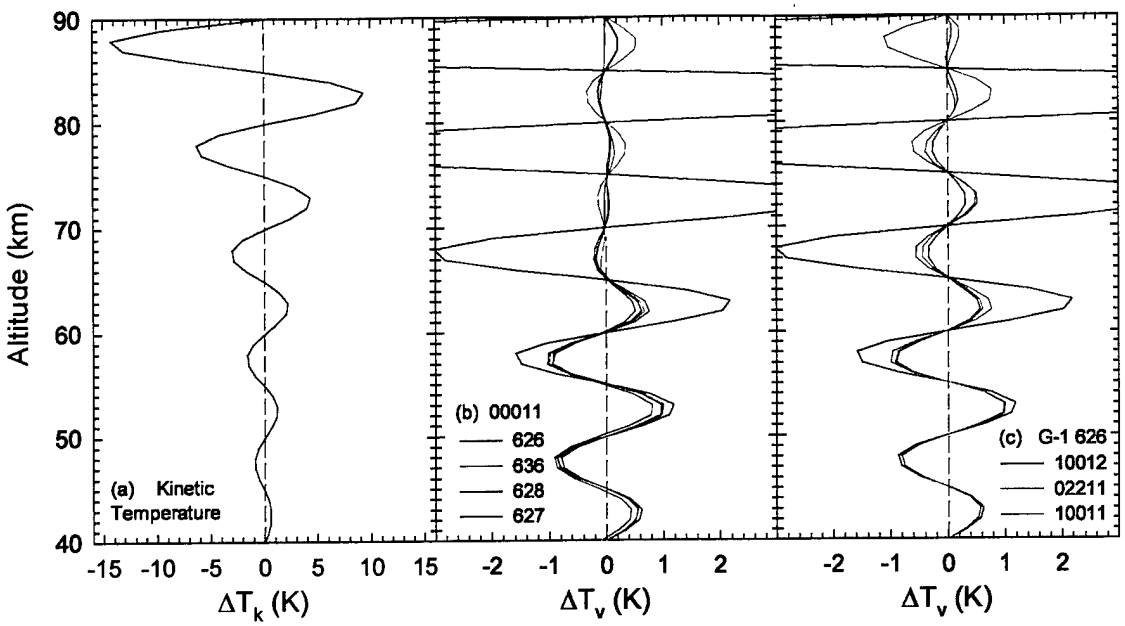


Figure 6. Wave-induced perturbations of (a) kinetic temperature; (b) vibrational temperature, $T_v$, of the $CO_2$(00011) state for four isotopes; and (c) $T_v$ for the Group 1 states of the 626 isotope. Most of the non-LTE contribution to the BTH radiance arises in these solar-pumped states near 80 km. The kinetic temperature perturbation is included in both (b) and (c) for comparison purposes.

result, the wave-induced excursions in temperature, which are much larger in the mesosphere than below the stratopause (c.f. Figure 3), have relatively little effect upon the emission rate. That is, even though the total modeled radiance is greater because of non-LTE emissions, the non-LTE component is relatively insensitive to temperature changes, and the radiance contrast between different LOS is determined primarily by the perturbation of the stratosphere rather than that of the mesosphere.

The effect of the relatively weak coupling between the kinetic temperature and the populations of the 4.3 μm states in the mesosphere is illustrated in Figure 6. We calculated vibrational temperatures of the most important emitting states in the presence of a wave, assuming daytime conditions with the Sun at a zenith angle of 60 degrees, and compared them with temperatures determined for the background atmosphere. Although the non-LTE model calculation is approximate, the wave-induced changes in vibrational temperature are much smaller than the changes in the kinetic temperature above 60 km, and indeed smaller than the changes in vibrational temperature at 40 km. Moreover, for various reasons, these temperature variations can have different phases with respect to each other in the mesosphere, so cancellation also occurs. Both of these circumstances underlie the conclusion that, despite the rapid growth of the wave amplitude in the mesosphere, its effect on the overall emission rate as integrated over the non-LTE segment of a BTH viewing path is small. More to the point, it is very small compared to effects from lower down where the densities are much greater and the CF has its maximum value.

There are several reasons that non-LTE results are approximate. One is that the horizontal spatial variations introduced by the wave cannot be accommodated in the radiative-transport calculation involved in determining the vibrational temperatures. For the non-LTE region the mean free path of photons in some 4.3 μm bands may be comparable

to the horizontal wavelength, so in the actual atmosphere there would be some averaging over regions with different emission rates. Another is that it is very difficult to calculate the solar flux absorption rates while taking into account the horizontal spatial variability. The calculations shown above assumed only vertical variations. Perhaps even more important, the non-LTE signal depends sensitively upon the actual growth of the wave, which is something that can be modeled only approximately in this region. Last of all, FASE does not correctly treat the minor isotopes in the non-LTE LOS calculation, since it assumes that their vibrational temperatures are the same as that of the major isotope.

For all of these reasons, it is very difficult to accurately simulate the non-LTE component of the BTH radiance in the presence of waves. We do know, at least for daytime conditions with a Sun angle of 75 degrees or less, that the overall non-LTE contribution is a significant portion of the total (as suggested by Figure 5) and therefore must be included in some fashion. Relying on the conclusion, stated above, about the diminished wave influence in the mesosphere, we explored the possibility of combining the non-LTE contribution from the background atmosphere with the LTE contribution in the wave-perturbed atmosphere to arrive at a proper simulated BTH radiance. However, that work is not complete, and a complete characterization of the non-LTE effects remains a matter for future consideration.

### 1.2 SABER

The phenomenological approach that we took toward studying atmospheric radiance structure involved the SABER instrument on the TIMED satellite. TIMED (Thermosphere Ionosphere Mesosphere Energetics and Dynamics) was launched in December 2001. SABER (Sounding of the Atmosphere using Broadband Emission Radiometry) is a 10-channel limb-sounding instrument whose overall purpose is to retrieve the temperature/pressure structure of the atmosphere, and to measure a number of emissions that are critical for determining the energy balance of the mesosphere/lower thermosphere (MLT) region. SABER provides nearly global coverage (either from ~52°S to ~82°N or from ~82°S to ~52°N) on a continual basis. It is developing a voluminous database of radiance profiles, which ultimately will be associated with an even more voluminous set of retrieved or derived quantities. The breadth and scope of the coverage that SABER is providing is unprecedented, for measurements of the MLT region.

One of the many things that will eventually be derived from the SABER data is a global picture of the radiance and radiance variability in each of its ten channels. The variability will be assessable on many of the different scales we outlined at the beginning of this section. When it is suitably organized and reduced into products that can be scanned in a systematic fashion, it will answer many outstanding questions about the frequency and magnitude of radiance perturbations, and will put limits upon what can be expected to be seen in the future.

As soon as Level 1B data (radiance data in physical units) were available, which was only very recently, we began a process of organizing the data set and looking at the radiance variability. We started with data from a single day, 3 March 2002. The set came from all 14 orbits that day, containing approximately 1360 events. An event is a single sweep of the sensors through a range of tangent heights from hard Earth to ~300-400 km. We looked at the $CO_2$ and OH channels. Channels 1-3, which have different passbands,

sense the 15 μm emissions that are used for (among other things) retrieval of kinetic temperature. Channel 7 measures 4.3 μm radiance, mostly from $CO_2$. Channels 8 and 9 detect $\Delta v = 2$ transitions from OH at 2.0 and 1.6 μm, respectively. For channel 8 these originate in vibrational states 8 and 9 (e.g., the 9-7 and 8-6 Meinel bands are seen) with a small contribution from $v' = 7$ as well. For channel 9 the bands are 5-3 and 4-2, with some 6-4 mixed in.

We have not looked at data from channels 4-6 (emissions from $O_3$, $H_2O$, and NO respectively) or at channel 10, which sees emissions from $O_2(^1\Delta_g)$ at 1.27 μm. In the ozone and water channels there are known issues concerning off-axis rejection that have not been resolved, and in any case other researchers are looking at these data in detail. The NO data, and $CO_2$ 4.3 μm data, are of particularly high quality. Usable data extend to much higher tangent heights than for any previously-accumulated data set, up to 250 km in the case of NO and 200 km for $CO_2$ in the daytime or when viewing active aurora.

The codes we used to perform the analysis that we present below, and that are capable of other tasks as well, are included among the software that is being submitted to the Air Force along with this report. Appendix A gives a short discussion of the tasks that these codes perform.

On the next two pages we show examples of typical SABER limb radiance scans for several of the channels we have been evaluating. Figures 7 and 8 show nighttime and daytime events from northern midlatitude regions. Figures 9 and 10 are for equatorial events. Parameters that we use to characterize each event–the SZA, latitude, etc.–vary over the extent of each limb path, and are also different for paths with different tangent heights. The values listed on the figures refer to the tangent point of the 80-km limb path in each case.

Figure 7 displays nighttime data from the four $CO_2$ channels and one OH channel for a midlatitude event. The 15 μm data on the right mostly reflect the thermal structure of the atmosphere. The protrusion that appears near 110 km is a common feature of SABER scans, and indeed similar features have been observed in past experiments. The signal to noise ratio exceeds 10 for tangent heights up to about 115 km, typical of SABER data. The 4.3 μm radiance on the left is affected by the kinetic temperature profile and many different processes, and includes small inband contributions from OH (9-8) and (8-7) emissions. Here the S/N exceeds 10 at 120 km. The OH profile is also typical of nighttime events.

Figure 8 shows a daytime midlatitude event. The channel-7 radiance is, as expected, one to two orders of magnitude higher than its nighttime value at all tangent heights in the mesosphere and thermosphere. In this case the useful data extend nearly up to 200 km. There probably is a contribution from $NO^+$ emission above 120 km.

Figure 9 is similar to Figure 7 but the data were acquired near the equator. The 15 μm radiances in channels 1-3 all have a very pronounced layer structure at 80 km, a feature that was seen in many low-latitude events on that day. The 4.3 μm and OH radiances also have maxima at this tangent height; in fact, the channel-7 radiance is a factor of five greater at 80 km than it is in the event shown in Figure 7. The 110-km feature in the 15 μm channels is less pronounced here than in the previous figures, but is still typical. Some events, however, have virtually no change of slope in this region.

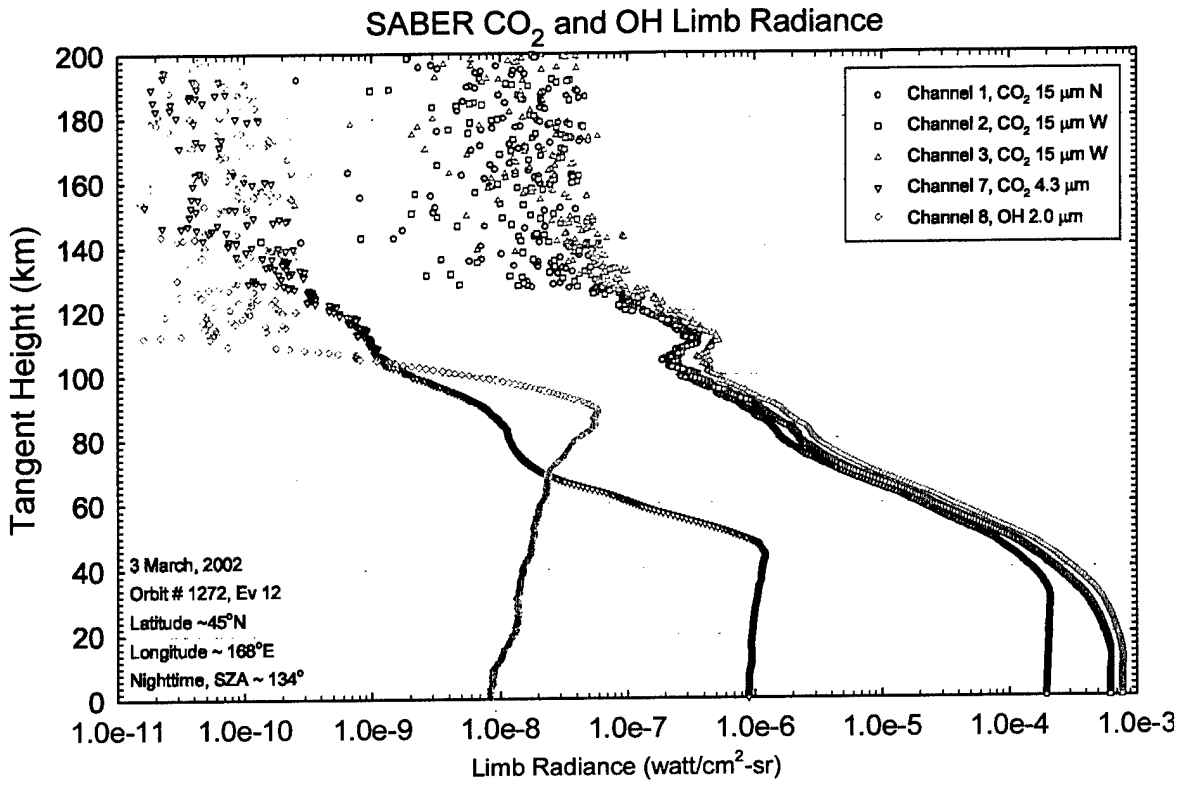


Figure 7. Typical midlatitude nighttime event, showing SABER radiances in $CO_2$ and OH channels.

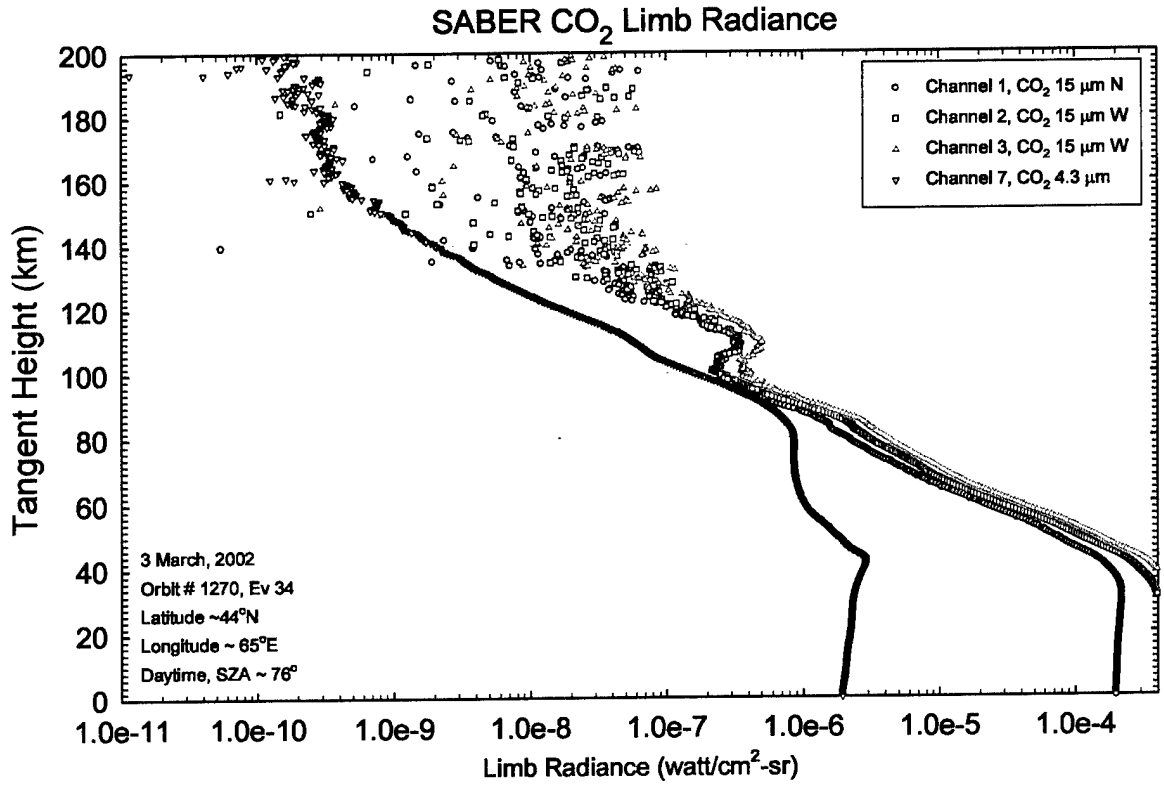


Figure 8. Typical daytime event, showing SABER radiances in the four $CO_2$ channels.

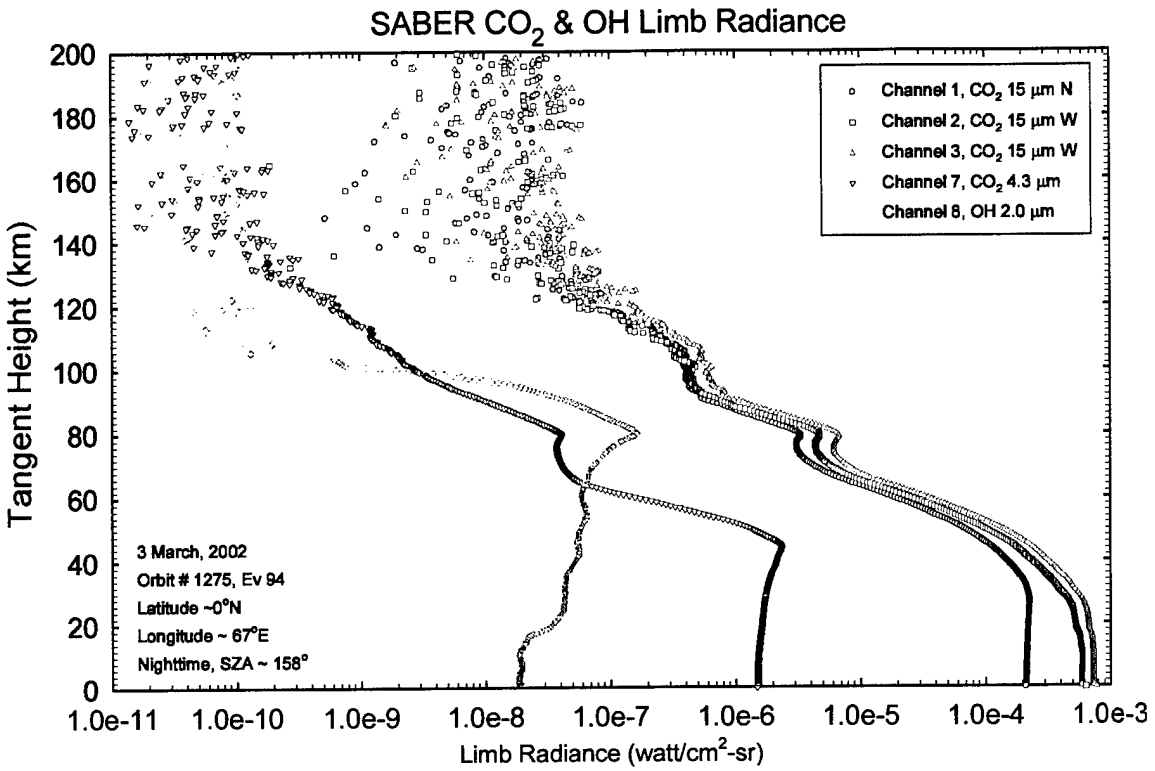


Figure 9. As Figure 7, but for an equatorial event

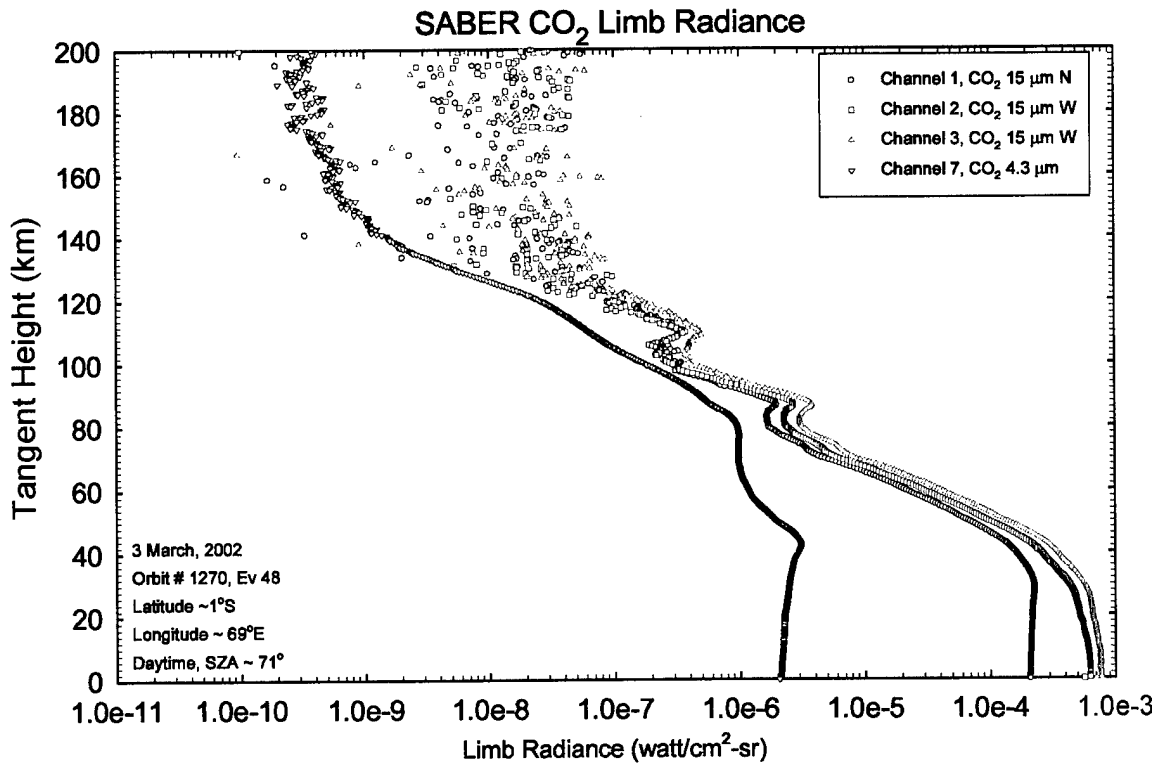


Figure 10. As Figure 8, but for an equatorial event.

Figure 10 shows a daytime equatorial event. One can see that the layer appearing in the upper mesosphere in the 15 μm channels in Figure 8 is also seen here, but at a somewhat higher tangent height (~88 km instead of ~80 km). Although not so prominent in all scans as in these two, this structure appears in most of the equatorial events that we examined among the March 3 data. The present interpretation is that it must be due to temperature inversion. In fact, preliminary LTE retrievals of temperature reveal this; for the event in Figure 10 an increase of ~60 K in $T_k$ is seen near 88 km. However, it must be noted that since non-LTE effects were not accounted for, all quantitative results like this are estimates that are likely to be changed considerably in the future. Moreover, day/night differences are suggestive of tidal effects, as discussed below.

We note that no correction for off-axis non-rejected earth radiance has been implemented in the version of the radiance data shown here. For some channels and some ranges of tangent heights, there are significant contributions from scattered light originating at low altitudes. The problem is most acute when the radiance profile drops sharply with increasing tangent height. The magnitude of corrections that will be made is not known at this time, but for future data releases reductions in limb radiance of as much as 50% are thought to be possible for the most strongly-affected channels. Since the corrections are likely to be similar for all similar events, the radiance variability that we observe will undoubtedly remain even after they are implemented. However, the absolute radiance levels may finally be quite different for some channels at some tangent heights.

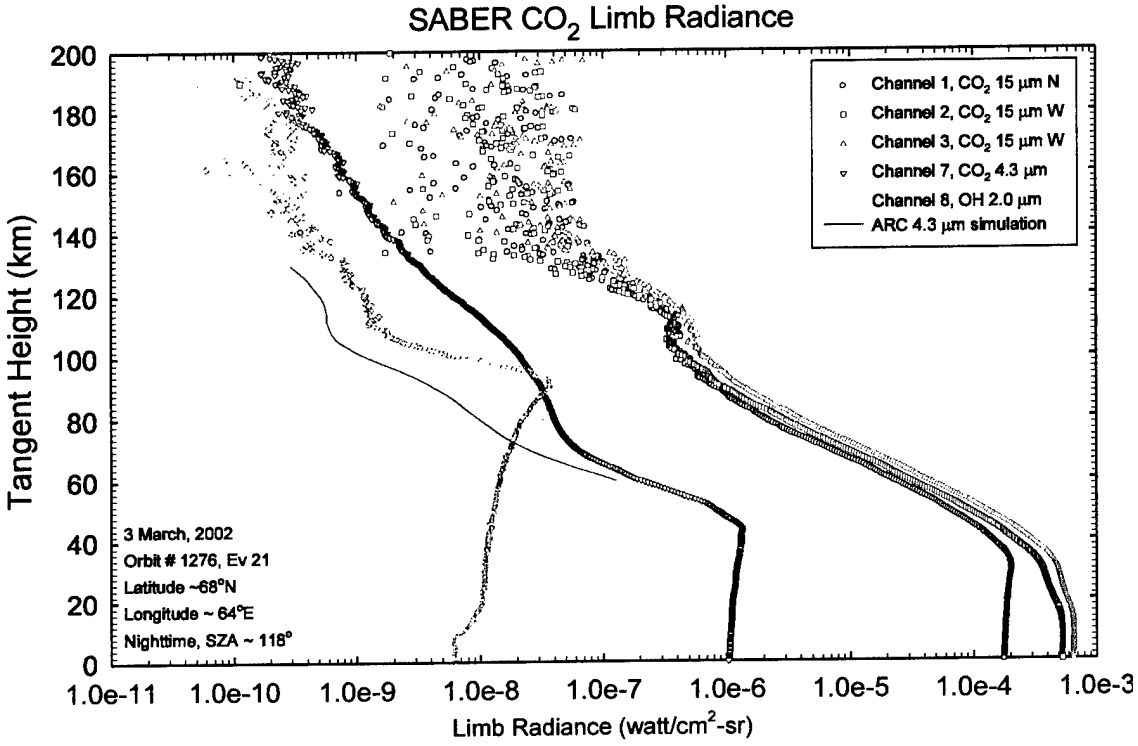


Figure 11. A nighttime high-latitude event, showing evidence of auroral excitation of the 4.3 μm states. A nighttime simulation assuming quiescent conditions is shown to illustrate the auroral enhancement.

Figure 11 shows a high-latitude event with a very large enhancement of radiance in channel 7, surely caused by an aurora. March 3 was a quiet day overall, but several high-latitude events show elevated channel-7 radiance, this being the most notable. The figure includes an ARC simulation of a quiet nighttime event to show the size of the effect. (The non-LTE calculation for that day gave excellent agreement with the 15 μm radiance, so that result is reasonably reliable.)

Modeling the 4.3 μm signature of an aurora is a very difficult task because of uncertainty about the level of dosing, and the location and extent of the dosing region along the LOS. In fact, a strong aurora on the far side of the tangent point produces only a very small change in radiance, due to atmospheric opacity, whereas the same dosing closer to the observing instrument could cause an enhancement of an order of magnitude as shown here, or possibly even more. Moreover, it is not clear how much of increases in radiance that are observed are due to directly-imaged aurora and how much may be due to ancillary effects from past activity, such as atmospheric heave. Nevertheless, it is useful to keep track of the extent by which these radiance levels vary.

Figure 11 also shows an enhancement in channel 8 radiance above about 100 km. This is seen in other high-latitude events and correlates with elevated 4.3 μm. It is unlikely that OH is making much of a contribution from these altitudes, but the actual source of the increase in 2 μm radiance has not been identified.

Just from looking at individual limb-scanning events, it is clear that a lot of variability exists even among events that one might expect to be alike–for example, nighttime events at similar latitudes, or consecutive events separated by relatively small distances. To assess this variability, we tried to devise ways of organizing and viewing data from many events at once. Figures 12-18 show one way of doing this. In these figures, we display averages, standard deviations, and minimum and maximum radiances calculated from the channel 1 (15 μm) data from all orbits of March 3, 2002, and the same for channel 7 (4.3 μm) nighttime data. Nighttime events were defined to be those for which the SZA at the 80-km tangent point was 105 degrees or greater. The figures break out the events according to latitude bins that together cover the full range of territory viewed by SABER on that day.

Note that averaging channel-7 daytime data would not be meaningful because of the large differences in the excitation of 4.3 μm states that is expected for the range of solar zenith angles encountered. The 15 μm states, on the other hand, do not respond directly to solar influences, so to first order one expects full-day averages of channel 1 data to be useful quantities. However, see the discussion below.

The first few figures in this compendium show data from low and mid latitudes. The northern midlatitude radiance (Figure 12) was apparently consistent over the globe, as the standard deviations and even the min-max envelopes suggest rather small excursions about the mean. This was less true at lower latitudes on that particular day (Figures 13-15). In that case, there were much larger deviations in the upper mesosphere in both channels between 30 degrees north and 30 degrees south, particularly in the bin spanning the equator, and the 15 μm radiance also has a great deal more variability near 110 km. In the lower mesosphere, on the other hand, there was remarkably little spread in the data in all these latitude bins. In the southern midlatitudes (Figure 16), there is less variability in

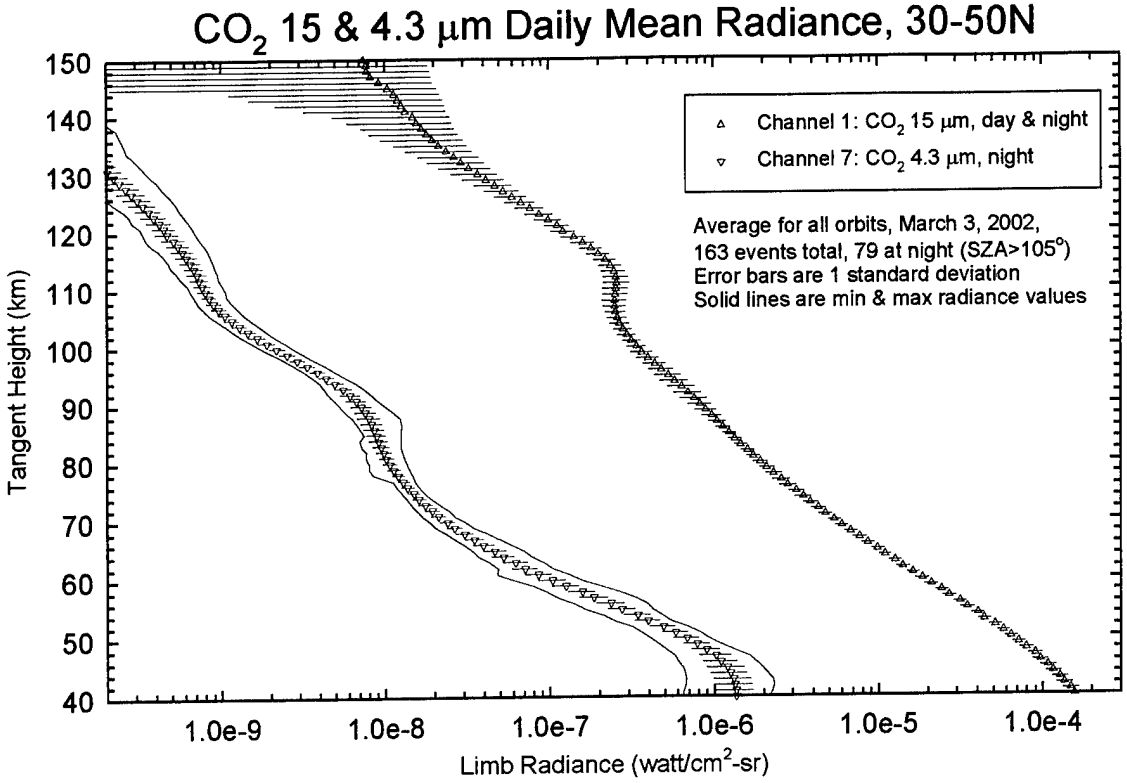


Figure 12. Average limb radiance, and standard deviation, for SABER channel 1 for all events in the latitude bin 30-50°N on March 3, 2002; and the same for channel 7 nighttime events. The solid lines give the radiance envelope, e.g. the minimum and maximum radiance from any event on that day.

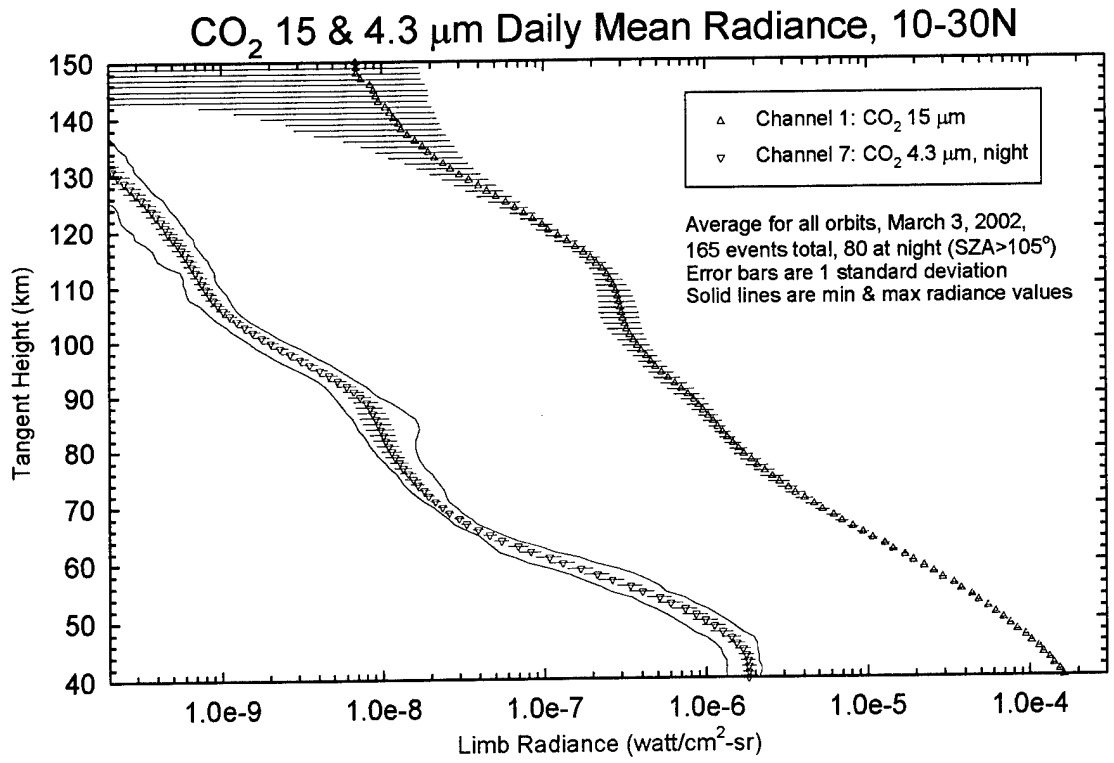


Figure 13. As Figure 12, but for the latitude bin 10-30°N.

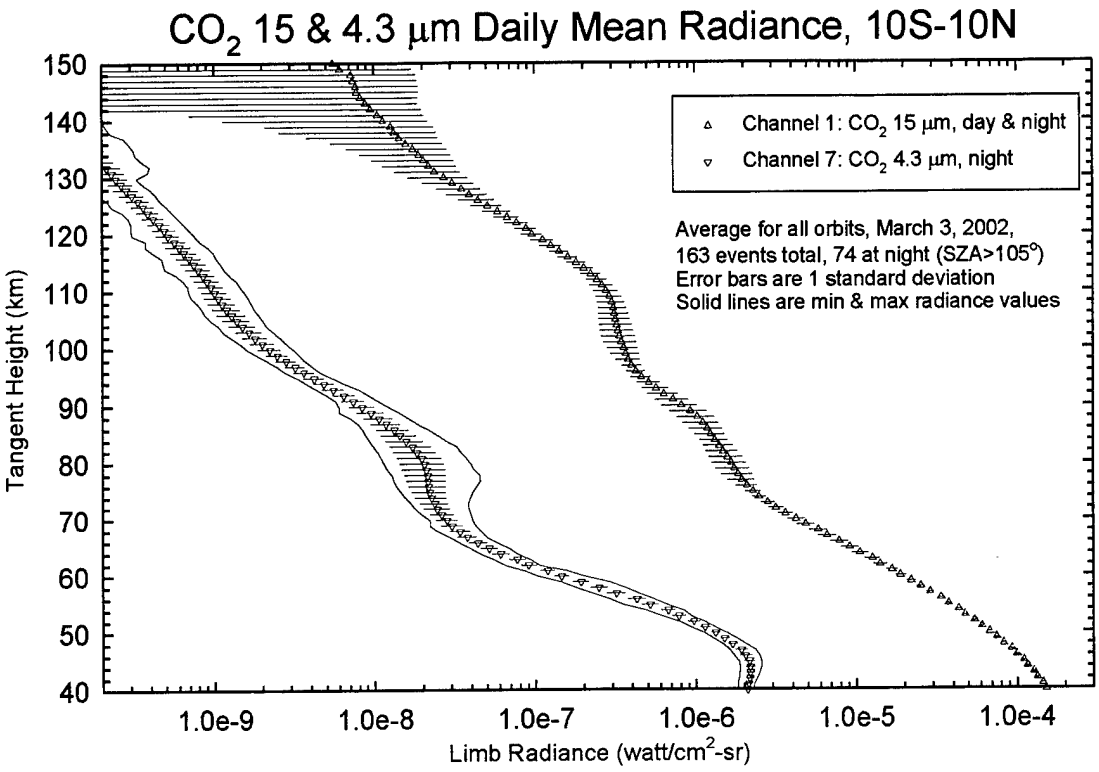


Figure 14. As Figure 12, bur for the equatorial latitude bin 10°S-10°N.

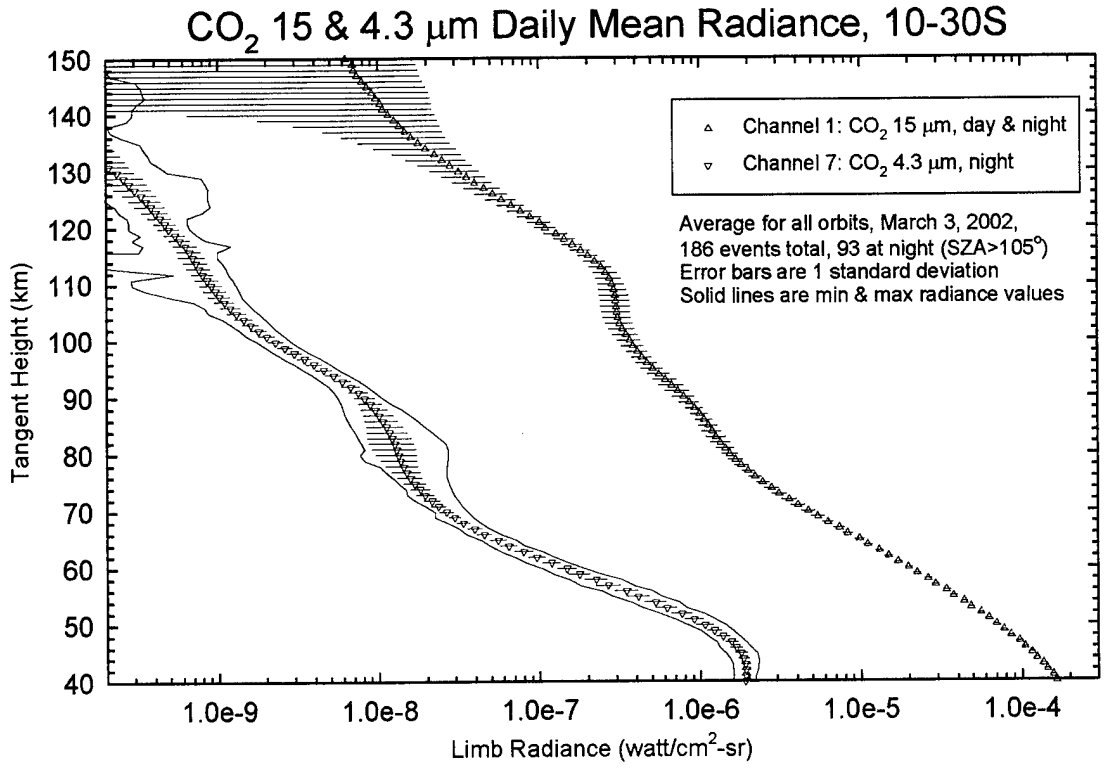


Figure 15. As Figure 12, but for the latitude bin 10-30°S.

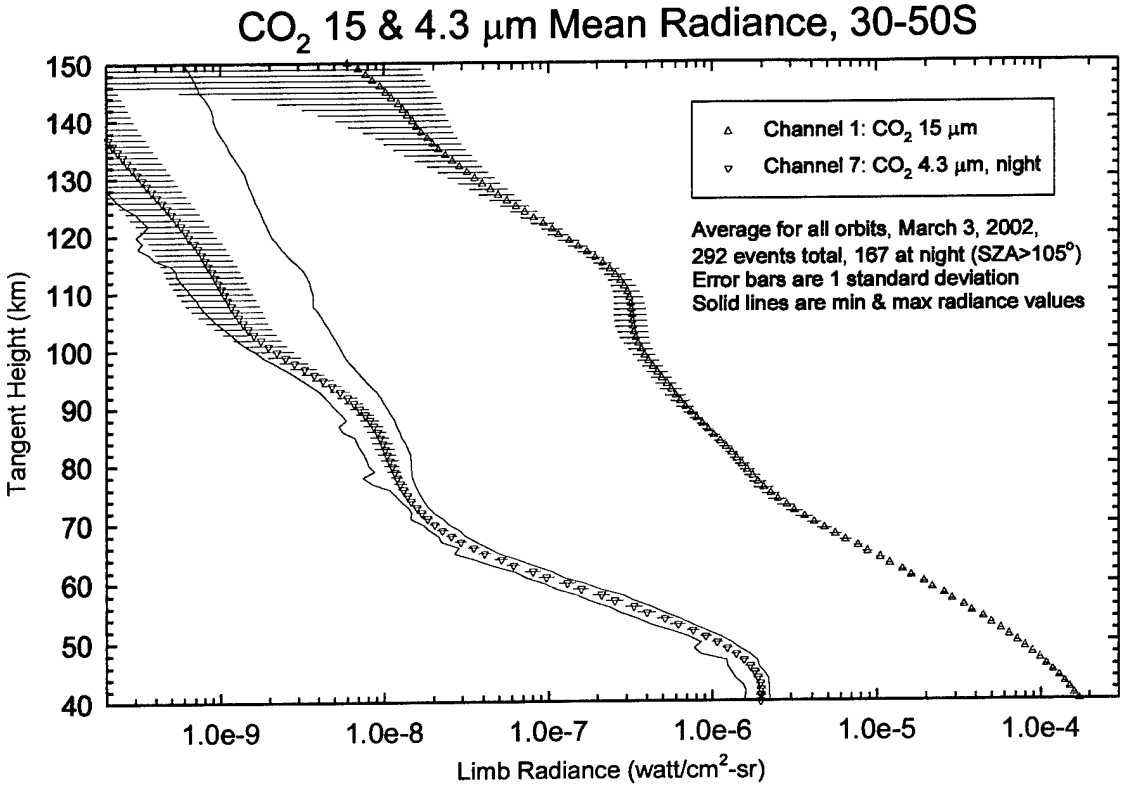


Figure 16. As Figure 12, but for the latitude bin 30-50°S.

the mesosphere. However, the 4.3 μm envelope shows a distinct skewing toward large radiance values at tangent heights above 90 km. This is due to one or possibly more events (but not many events) that viewed regions with auroral excitation.

In the high northern latitudes (Figures 17 and 18), there is ample evidence of auroral excitation. Not only is the envelope greatly skewed to high radiance, but the standard deviations fall outside the envelope on the low-radiance side. This is a consequence of averaging over two distinct populations, which makes the quantities plotted less meaningful than they would otherwise be. The continued need to look at high latitudes makes it desirable to find some way of identifying events with auroral influences among the SABER data, so that statistics could be calculated for quiescent events alone and occurrence probabilities for auroras of different apparent strength could also be determined. The best way to do that would be with correlative data from UV or visible sensors, but the only instrument providing such data consistently is the Global UltraViolet Imager (GUVI) on board TIMED. Since GUVI's views are not coincident with those of SABER most of the time, and since in any case no algorithm has been developed for accomplishing this, the use of SABER data alone is preferable. A very crude attempt to develop an auroral discriminant based on channel 7 data is described below.

It is worth noting, in Figures 17 and 18, the large spread in 4.3 μm radiance at tangent heights of ~40-55 km. This was not seen in lower latitude regions on this day. It is likely due to variability in the stratopause temperature, but it is interesting that it is not apparent in the 15 μm data.

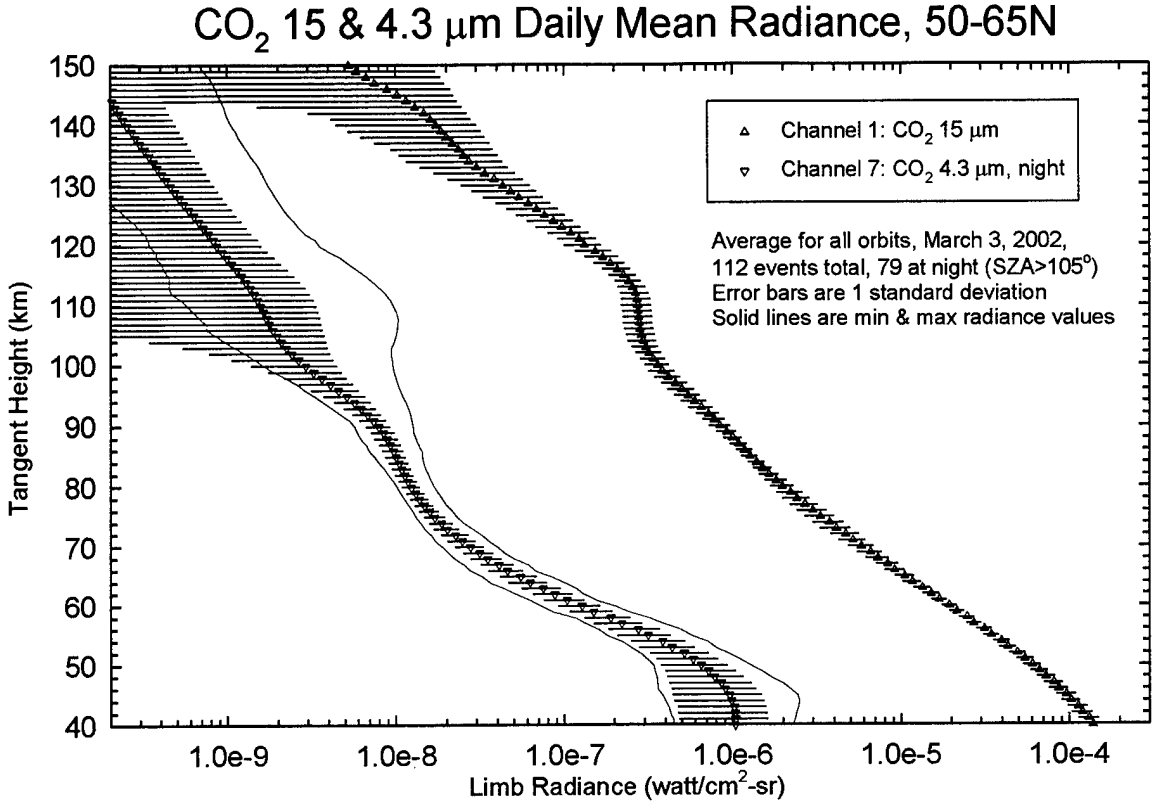


Figure 17. As Figure 12, but for the latitude bin 50-65°N. Auroral effects skew the channel-7 statistics, as discussed in the text.

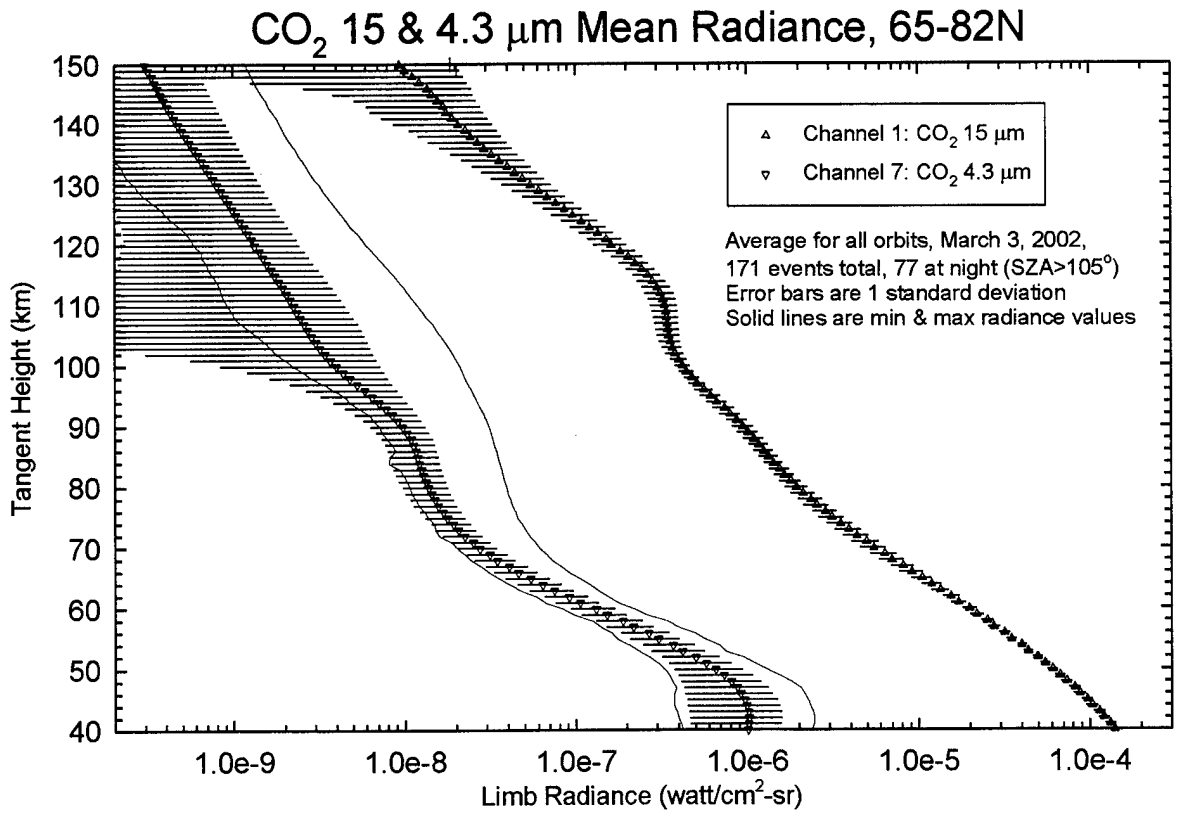


Figure 18. As Figure 17, but for the latitude bin 65-82°N.

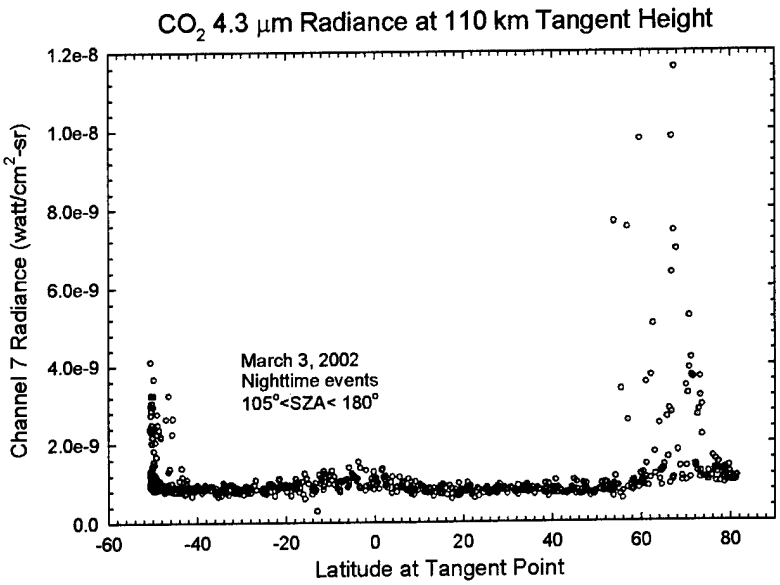


Figure 19. Latitude distribution of channel-7 radiance at 110 km, for all nighttime events of March 3, 2002.

Earlier, we mentioned the need for an indicator of auroral dosing. Figure 19 shows the distribution in latitude of channel-7 radiance at 110 km for March 3. One can see greatly elevated radiance levels for events poleward of 50 degrees in each hemisphere. We have made use of these data to develop an *ad hoc* auroral discriminant. The procedure consists of least-squares fitting the low-latitude data to a tenth-order polynomial, determining the standard deviation of these points with respect to the fit, and then asserting that any high-latitude event with radiance greater than five standard deviations beyond an extrapolated baseline is an "auroral event". The reason for using a polynomial can be seen in the shape of the data near the equator, where there is a small

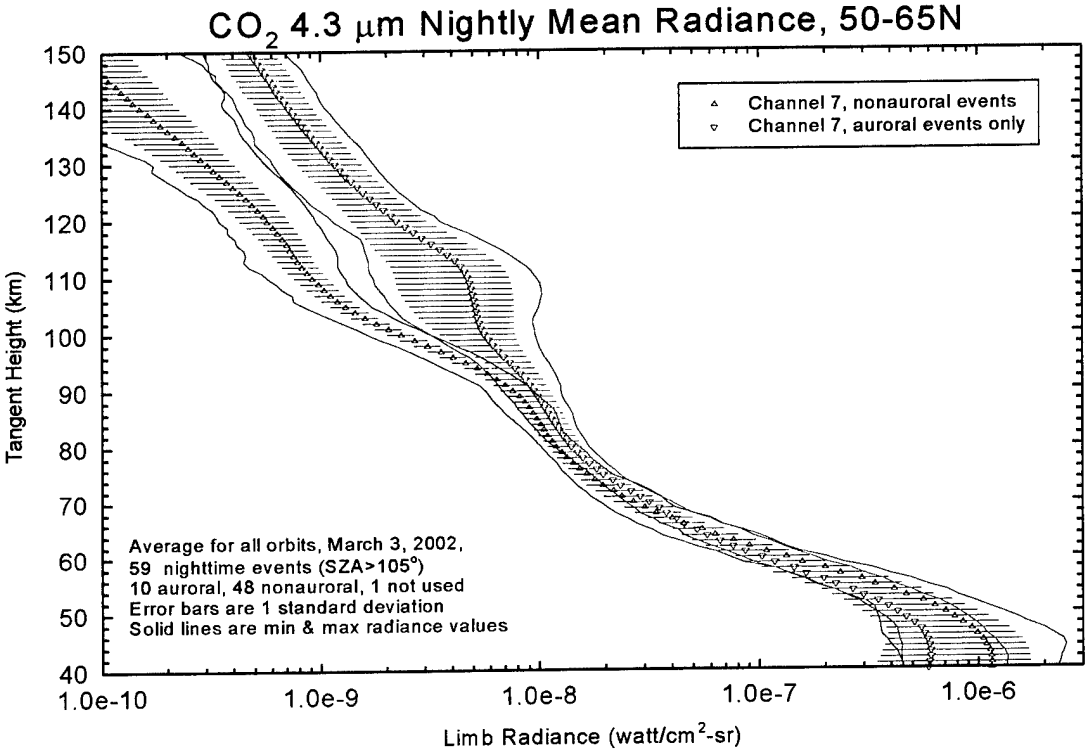


Figure 20. Channel-7 average and standard deviations, distinguishing between auroral and non-auroral events.

but significant variation with latitude. We also note that the extrapolation to high latitudes simply uses a constant value at each end. And finally, deviations from fits from several different tangent heights above 100 km, not just the one shown, were taken for each event in an attempt to get a less arbitrary index. Nevertheless, a considerable degree of arbitrariness does still attach itself to the procedure.

Figure 20 shows that, for channel 7 at least, two distinct populations of events can be distinguished by our *ad hoc* approach. Considering what was done, that would certainly be expected. In Figure 21 we show, however, that other SABER data are correlated with the "strength" of an auroral event, defined by a number of standard deviations by which a given event's channel-7 radiance exceeds the high-latitude baseline at several tangent heights. This plot gives channel-8 data for a day in April 2002 when a solar storm was in progress and when, therefore, there were many more high-latitude events with elevated radiance. We do not plot the one-sigma bars for the "moderate" and "strong" auroral events because they are so large that they overlap and would obscure each other. The fact that they are so large is suggests that the correlation between "strong" auroral signatures in channels 7 and 8 is poor, and likewise between "moderate" ones. This is what would be expected for localized sources, in consideration of the fact that one emission is optically thick and the other is not, and also of the fact that the index we have defined has only the most tenuous connection with physical processes that produce strong and weak aurora. Nonetheless, one can see from Figure 21 that there is at least some utility in trying to make the distinction. One point is that the entire SABER data set can be examined with this discriminant, without resort to incomplete or hard-to-obtain ancillary data.

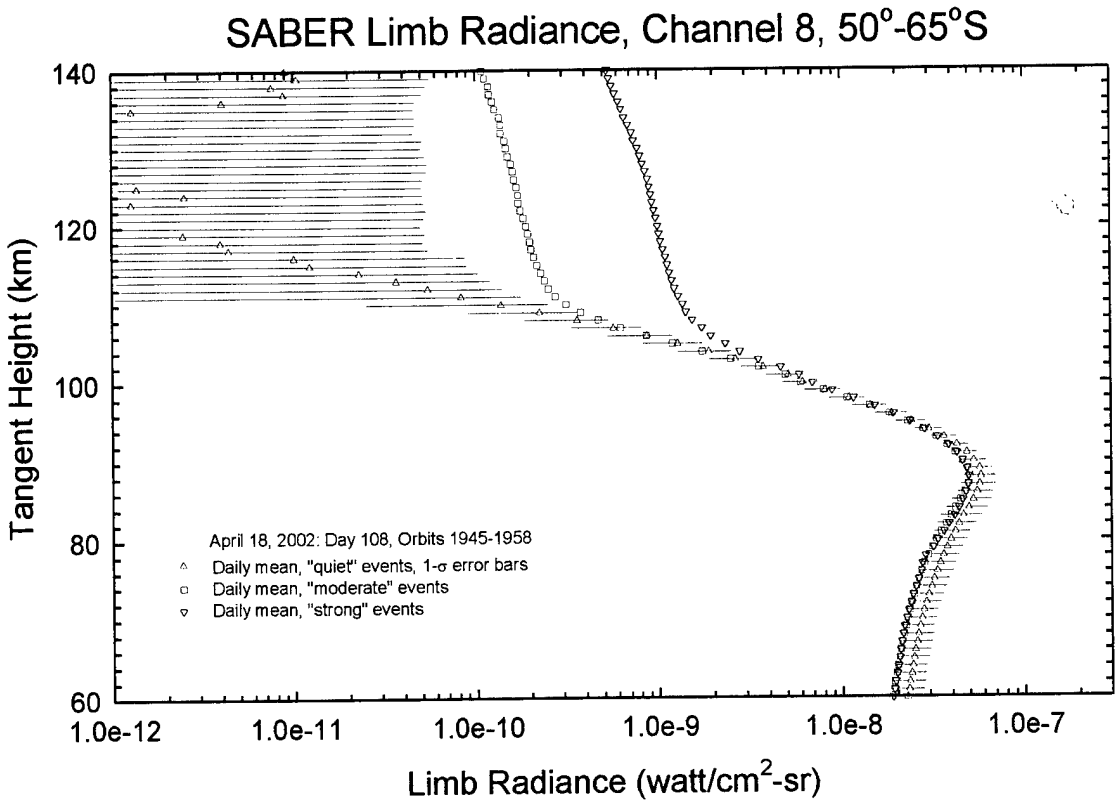


Figure 21. OH data from an active day in April 2002, distinguishing quiescent events from those viewing "moderate" and "strong" auroras according to the index discussed in the text.

We investigated one other aspect of the March 3 data that was only briefly touched upon in the earlier discussion. The peaks and slope changes in the 15 μm radiance profiles that are seen in many of the equatorial events on that day (as in Figures 9 and 10) suggest that temperature inversions are ubiquitous in the upper mesosphere in this geographical region. Moreover, the peaks typically appear at different tangent heights in daytime and nighttime. To get a more complete picture, we averaged daytime and nighttime scans separately and compared the averages. The results for the equatorial latitude bin are given in Figure 22, in a fashion similar to that of Figures 12-18. Note that the nighttime error bars have small caps, whereas (in order to avoid cluttering the plot) the daytime ones do not. A plot of the day/night difference as a percent of the daily mean (including night and day) is also included. The local time at the ascending and descending nodes was approximately 1700 and 0200, respectively, for all orbits.

The day/night differences in Figure 22 are striking. Since the 15 μm radiance is determined primarily by the thermal structure of the atmosphere, one must conclude that the wavelike radiance pattern, with the day and night profiles apparently just out of phase with each other, is a manifestation of the diurnal tide. However, confirmation of that conclusion requires detailed modeling, which we have not done. When reliable retrieved temperature profiles become available, it should be possible to be more definite.

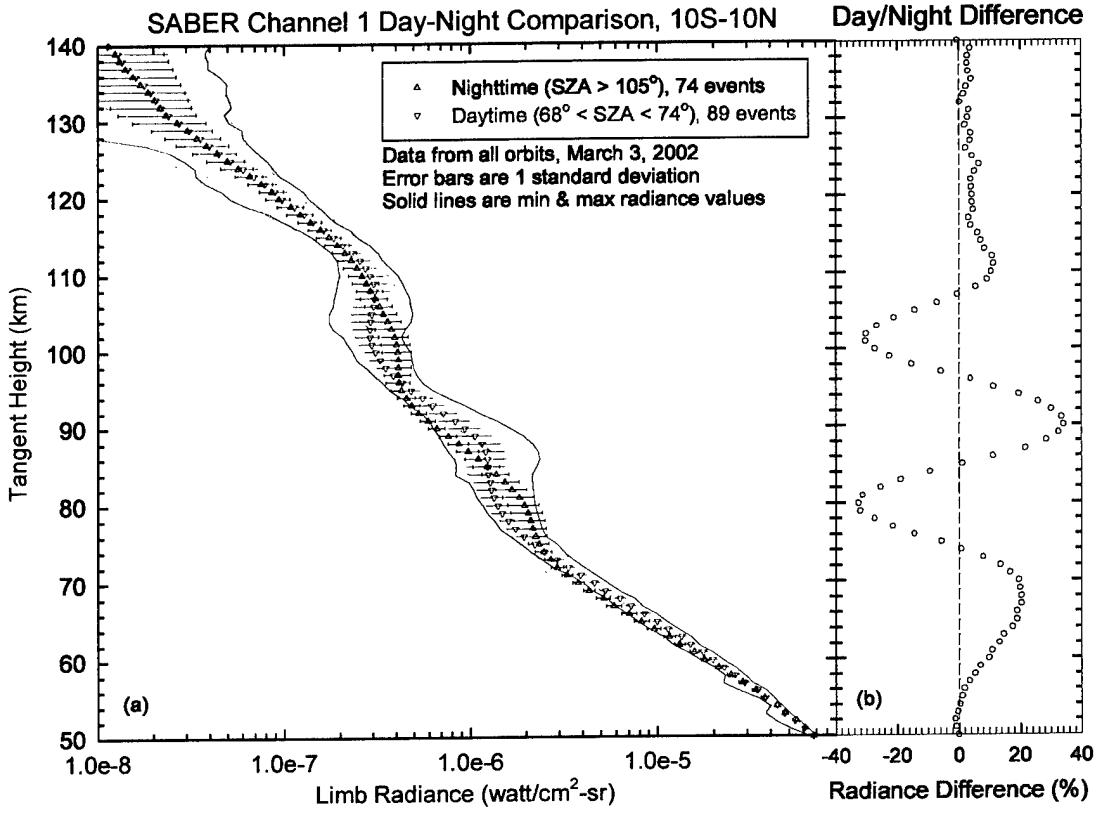


Figure 22. (a) SABER 15 μm limb radiance in the latitude bin spanning the equator for March 3, separately averaged over all daytime and nighttime events. Error bars indicate one standard deviation in each case. (b) percent difference (day minus night) expressed as a percentage of the total daily mean radiance.

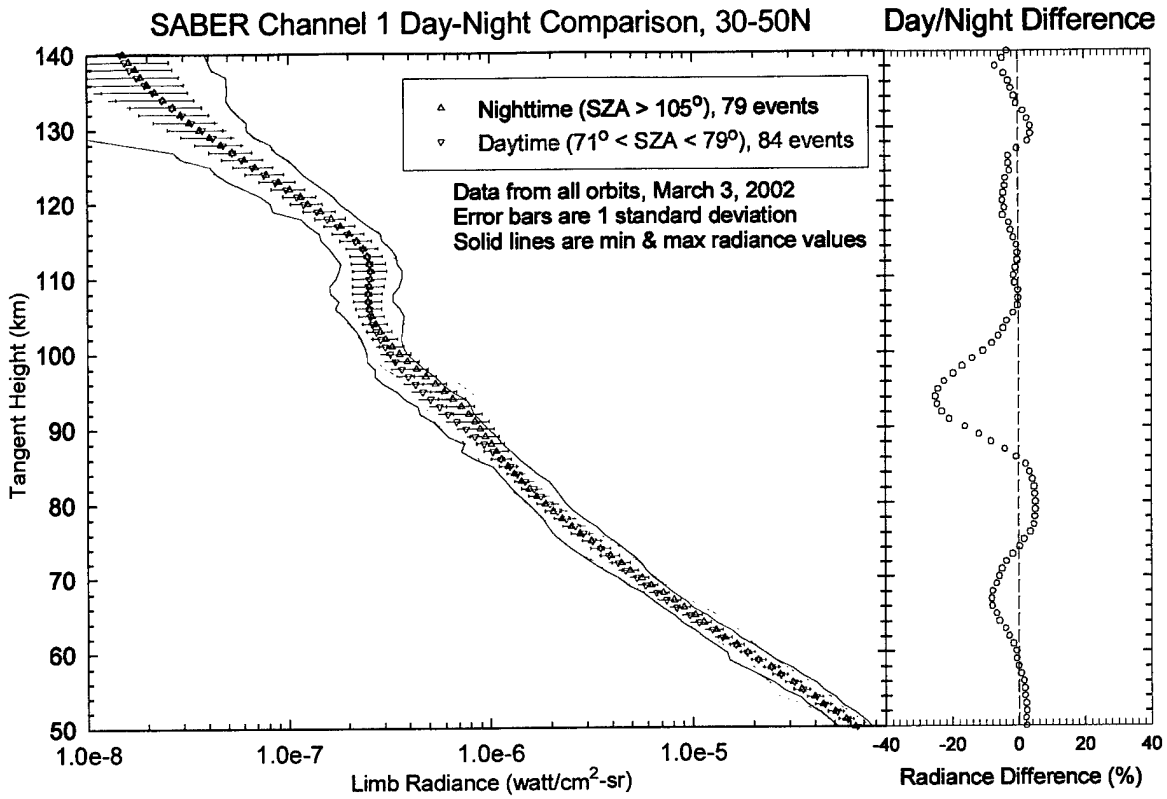


Figure 23. As Figure 22, but for the northern midlatitude region.

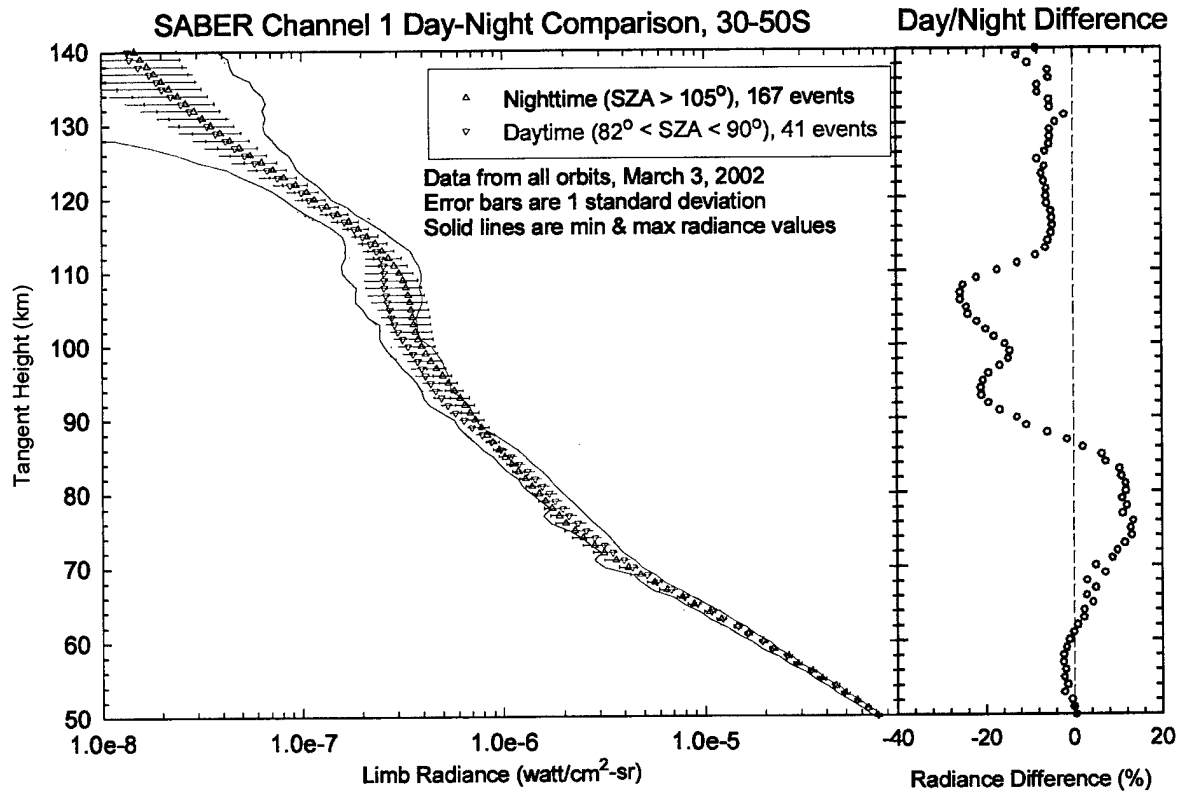


Figure 24. As Figure 22, but for the southern midlatitude region.

Figures 23 and 24 present similar results for northern and southern midlatitude regions, respectively. For midlatitudes one expects the semidiurnal tide to dominate, and indeed the day/night differences do not resemble the structures seen for the equatorial region in Figure 22. However, we reiterate that the role that tidal processes may play in determining the 15 μm radiance has not been investigated in detail, and comments relating to it remain quite speculative.

It is interesting to note in Figures 23 and 24 that the nighttime average radiance exceeds the daytime average radiance near the mesopause. All other things being equal, one expects non-LTE effects to produce exactly the opposite result in this region. In the daytime, energy transfer from solar-pumped 4.3 and 2.7 μm states to the bend-stretch manifold elevates vibrational temperatures of some of the 15 μm states by ~4-7 K for typical midlatitude conditions, compared to nighttime. This produces an increase in limb radiance of ~5%. (For cold polar summer conditions, much larger effects would be expected.) Therefore, the SABER results show that all other things are *not* equal, moreover that the underlying conditions of the atmosphere counteract and overwhelm the non-LTE effects.

The figures presented in this section barely scratch the surface of the information that will ultimately reside in the SABER database. The radiance data alone will provide a very complete picture of global radiance variability in much of the infrared spectral region. Quantities that will be retrieved from them (such as temperature, minor constituent densities, cooling rates, etc.) will constitute an additional unprecedented and very rich resource for research on the MLT region.

## 2. Atmospheric Radiance Code (ARC)

During the development of its temperature and constituent-density retrieval algorithms, the SABER project required a considerable amount of detailed non-LTE modeling. This was done to insure that the operational code would incorporate the best forward calculations that could be performed, and to determine systematic and random errors that could result from uncertain input parameters (for example, rate constants) or imprecise numerical procedures. Benchmark calculations for many $CO_2$ states were performed using our non-LTE model, Atmospheric Radiance Code (ARC); some of them were discussed by Wintersteiner [*2001*]. The need for accurate results prompted us to write and check two new codes, which are described very briefly below.

### 2.1 RADV

RADV is a new component of ARC. It replaces much of the functionality of an older code, VPMP. Its purpose, like that of RAD and RADC [*Wintersteiner et al, 1996*], is to calculate vibrational temperatures of certain $CO_2$ states. In this case, the states are the so-called "Group 1" {10012-02211-10011} and "Group 2" {11112-03311-11111} states, which lie approximately 3600 and 4300 $cm^{-1}$ above ground, respectively. They are strongly coupled to each other, and also to ground or lower-lying $CO_2$ states by radiative transitions and by fast V-V exchange with $N_2$.

The basic difference between RADV and VPMP is the inclusion of radiative transfer within the atmosphere in the new code, leading to more accurate excitation rates for the states in question.

In the daytime the principal excitation mechanism for the states of Groups 1 and 2 is solar pumping at 2.7 μm. Once excited, they emit photons at both 4.3 and 2.7 μm. This contributes heavily to the total emission at 4.3 μm, and even, indirectly, to emission at 15 μm (because the lower states of the 4.3 μm transitions are in the bend-stretch manifold). They also affect the population of vibrationally-excited $N_2$, which feeds back and in turn influences the populations of other $CO_2$ states that emit at 4.3 μm. The daytime problem was discussed in considerable detail by Sharma and Wintersteiner [*1985*], among others. At night, there is no strong excitation mechanism, and these states are often ignored.

The need to model the emission at 4.3 μm very accurately caused us to study the effect of radiative transfer in 2.7 and 4.3 μm bands on the populations of the Group 1 and 2 states. Previously neglected because of the dominance of solar excitation in daytime and the relative unimportance of these states at night, this process was included in RADV using the basic ARC algorithm for radiative transfer [*Wintersteiner et al, 1992*]. Each group is connected to lower states through two 2.7 μm bands and three 4.3 μm bands. The results show that the latter are considerably more important than the former for exciting the high-lying states.

In the daytime, the inclusion of this additional excitation mechanism increases the vibrational temperatures of the three Group-1 states by approximately 2 K in the lower mesosphere, but only for the major (626) isotope as shown in Figure 25. This produces a minor but not negligible enhancement in the total 4.3 μm limb radiance near 65 km. For the minor-isotope and Group 2 states, the changes amount to less than half a degree in the mesosphere. Because these states have much lower absolute densities, the resulting effect

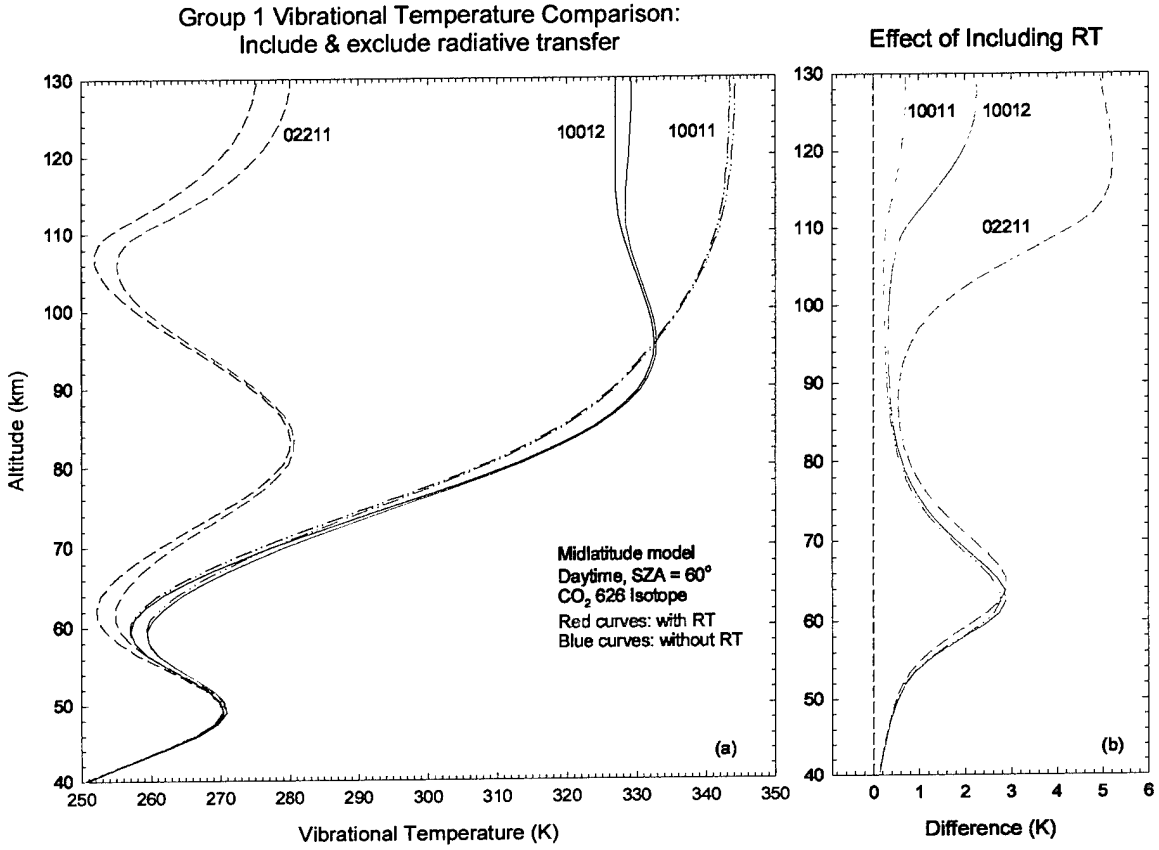


Figure 25 (a) Typical daytime vibrational temperatures of the $CO_2$ major-isotope (626) Group 1 states, calculated with and without radiative excitation from within the atmosphere. (b) Differences in vibrational temperature between the two cases.

on the radiance is extremely small. The increases that are seen at much higher altitudes, in the thermosphere, also have negligible impact.

For the nighttime calculation, in contrast, the inclusion of radiative transfer is necessary for a realistic result. Whereas the Group-1 major-isotope states add only a few percent to the total 4.3 μm limb radiance at tangent heights in the lower mesosphere, it is still worthwhile to have the capability to figure their contribution.

RADV replaces VPMP for purposes of calculating the populations of Group 1 and 2 states, but the latter code is still used for the higher-lying Group 3 states. In daytime, these are solar-pumped at 2.0 μm as well as at 2.7 and 4.3 μm, and the radiative-transfer contribution is likely to make very little difference Their significance at night is completely nil.

## 2.2 OH_MODEL

OH_MODEL is another new component of ARC. It performs a very simple calculation of the populations of vibrational states of the OH ground electronic state, following chemical production by the so-called "H plus $O_3$" reaction:

$$H + O_3 \rightarrow OH(v) + O_2 \qquad v \leq 9$$

The motivation for developing this code was threefold: to model the SABER limb radiance in channels 8 and 9, which capture Δv=2 emissions from OH; to model the contribution of Δv=1 emission from OH in SABER channel 7; and to calculate the effect that OH may have on the $N_2$ and $CO_2$ nighttime vibrational populations through V-V transfer, according to a long-standing hypothesis of Kumer [*1978*]. Work making use of these capabilities is ongoing but incomplete. We also used OH_MODEL to check results from the SABER operational code, by running cases with the same input.

The new code requires that one specify the input model atmosphere plus the density profiles of both atomic hydrogen and ozone. It determines the rate of production of the nascent states (v=6 through v=9), and the production and loss rates of every level due to collisional and radiative processes, and performs a steady-state calculation by equating production and loss. The quenching scheme follows the prescription of Adler-Golden [*1997*] and the Einstein coefficients are from Goldman et al [*1998*]. The correct values for all the parameters involved is still a matter of some uncertainty, and indeed has been explored by others at considerable length. However, we did not do any systematic study along those lines; instead we relied on what had already been done.

The results that we obtained with OH_MODEL are entirely as expected. The altitude of the OH layer that it predicts depends on the input profiles of H and $O_3$, as do the number densities that it calculates. The relative state-to-state populations depend primarily on the quenching scheme and the Einstein coefficients. There was excellent agreement with the SABER operational code, as anticipated. The code is now an accepted component of ARC, and is included as a deliverable to AFRL, as indicated in Appendix A.

## 3. Summary

During the period covered by this contract, we have made considerable technical progress on several fronts in fields that are of interest to the Air Force. The major advances are detailed in the first technical section of this report, Section 1.

We have conducted two rather different investigations of atmospheric radiance clutter. In the first, we studied atmospheric gravity waves from a physics standpoint in order to develop a capability for predicting upwelling wave-generated radiance in the $CO_2$ 4.3 μm band. There were several motivations for doing this. One was to replicate MSX data obtained in 1996 with downlooking instruments and thereby improve our understanding of processes involved, including non-LTE processes. Another was to model the conditions and viewing geometry for which waves could be expected to be seen, in general. Although we did not discuss it explicitly in our report, a third motivation was to guide the planning for a proposed satellite mission dedicated to studying atmospheric gravity waves, Waves Explorer.

The other investigation took the rather different tack of examining new infrared radiance data obtained by the SABER instrument aboard the TIMED satellite. In this case, the idea is to look at mean radiance and radiance variability over the globe for different geophysical conditions. The ultimate purpose would be to catalog these results for the full range of latitudes, seasons, local time, solar activity, etc., or at least as much of those ranges as will eventually be represented in the database. The work reported in Section 1.2 makes use of only a single day's worth of data from early in the mission, but it shows results that are (presumably) typical near equinox. We have given typical radiance profiles, and daily or nightly means, and discussed their characteristics. We specifically pointed to effects caused by auroral activity and (we believe) tidal perturbations.

The more important codes that we have developed in the course of our investigations have been made available to researchers at the Air Force Research Laboratory, along with supporting files and documents. They have been delivered in the form of source modules, as outlined in Appendix A. The two new components of ARC are described briefly in Section 2. We have also engaged in discussions about how best to use all the codes, and what further development of them would be most useful in the future.

## References


Adler-Golden, S., 1997, "Kinetic parameters for OH nightglow modeling consistent with recent laboratory measurements," *J. Geophys. Res.*, **102**, 19969-19976.

Clough, S.A., Kneizys, F.X., Shettle, E.P., and Anderson, G.P., 1986, "Atmospheric Radiance and Transmittance: FASCOD2," *Sixth Conference on Atmospheric Radiation*, pp.141-144, American Meteorology Soc., Boston.

Dewan, E.M., Picard, R.H., O'Neil, R.R., Gardiner, H.A., Gibson, J., Mill, J.D., Richards, E., Kendra, M., and Gallery, W., 1998, "MSX satellite observations of thunderstorm-generated gravity waves in mid-wave infrared images of the upper stratosphere," *Geophys. Res. Lett.*, **25**, 939-942.

Gardiner, H.A.B., O'Neil, R.R., Grieder, W., Hegblom, R., Humphrey, C., Stair, A.T., Gallery, W.O., and Sears, R., 1994, "Midcourse Space Experiment (MSX): Planned observations of MWIR BTH and LATH backgrounds," *Proc. Soc. Photo. Opt. Instrum. Eng.*, **2223**(25), 274-285.

Goldman, A., Schoenfeld, W.G., Goorvitch, D., Chackerian, C., Dothe, H., Melen, F., Abrams, M.C., and Selby, J.E.A., 1998, "Updated line parameters for $OH(X^2\Pi)(v',v'')$ transitions," *J. Quant. Spectrosc. Radiat. Transfer*, **59**, 453-470.

Kumer, J.B., Stair, Jr., A.T., Wheeler, N., Baker, K.D., and Baker, D.J., 1978, "Evidence for an $OH^* \rightarrow N_2^* \rightarrow CO_2(\nu_3) \rightarrow CO_2 + h\nu$ (4.3μm) mechanism for 4.3-μm airglow,", *J. Geophys. Res.*, **83**, 4732-4747.

Picard, R.H., O'Neil, R.R., Gardiner, H.A., Gibson, J., Winick, J.R., Gallery, W.O., Stair, Jr., A.T., Wintersteiner, P.P., Hegblom, E.R., and Richards, E., 1998, "Remote sensing of discrete stratospheric gravity-wave structure at 4.3 μm from the MSX satellite," *Geophys. Res. Lett.*, **25**, 2809-2812.

Picard, R.H., Winick, J.R., and Wintersteiner, P.P., 2002, "Non-equilibrium radiative transfer in structured atmospheres," *Proc. SPIE*, **4539**, Remote Sensing of Clouds and the Atmosphere VI, 454-468.

Sharma, R.D., and Wintersteiner, P. P., 1985, "$CO_2$ component of daytime Earth limb emission at 2.7 micrometers," *J. Geophys. Res.*, **90**, 9789-9803.

Walterscheid, R.L., Schubert, G., and Straus, J.M., 1987, "A dynamical-chemical model of wave-driven fluctuations in the OH nightglow," *J. Geophys. Res.*, **92**, 1241-1254.

Winick, J.R., Picard, R.H., Wintersteiner, P.P., and Makhlouf, U.B., 2001, "Space-based observation of gravity wave induced radiance fluctuations: Simulation and MSX observations," *EOS Trans. AGU*, **82**, S278.

Wintersteiner, P.P., 2001, *Observations and Modeling of Atmospheric Radiance,* AFRL-VS-TR-2002-1586.

Wintersteiner, P.P, Paboojian, A.J., and Joseph, R.A., 1996, *Studies of Non-LTE Atmospheric Emissions: Modeling and Data Analysis*, PL-TR-96-2226.

Wintersteiner, P.P., Picard, R.H., Sharma, R.D., Winick, J.R., and Joseph, R.A., 1992, "Line-by-line radiative excitation model for the non-equilibrium atmosphere: application to $CO_2$ 15 μm emission," *J. Geophys. Res.*, **97**, 18083-18117.

Wintersteiner, P.P., and Sharma, R.D., 1985, *Update of an Efficient Computer Code (NLTE) to Calculate Emission and Transmission of Radiation Through Non-equilibrium Atmospheres*, AFGL-TR-85-0240, Air Force Geophysics Laboratory Technical Report.

# APPENDIX A: ARC AND SABER COMPUTER CODES

This Appendix gives a brief description of the contents of the ZIP disk that has been delivered to satisfy one of the Contract Data Requirements, "computer software product end items". The disk was written under LINUX but should be readable by Windows machines as well.

## A.1 ARC

The current version of Atmospheric Radiance Code (ARC) can be found in the subdirectories of the first-level directory, ARC. As indicated in the table below, there are eight such subdirectories. These correspond to the seven primary codes that comprise ARC, plus the convolution program CONV. Each of the first seven contains all the source code that is necessary for running that program, as well as a makefile that can be used to produce an executable. There are between three and seven source files in these subdirectories, each of them containing one or more concatenated source modules. The name of the subdirectory indicates what the current version number is for each code.

Table A-1: ZIP Directory Structure

```
/
  ARC
        RAD_53
        RADC_17
        RADV_3
        SABS_15
        VPMP_10
        OHMOD_1
        NLTEA_13
        CONV_9
  SABER
        READ_SDAT_6
        RAD_DIST_5
```

Each main ARC subdirectory also contains examples of so-called directives files. These are used to specify how the respective programs operate: which options to invoke, which input files to use, what geophysical information to use, what values to use for each program parameter, and what names to give the output files. These are referred to as "unit-1 files" because they are associated with logical unit 1 in each code, and they have names with the program name and the mnemonic "001" in them. For example, "rad001_nu2_n.dat" is a sample directives file for the nighttime $CO_2(\nu_2)$ calculation performed by RAD.

The CONV subdirectory contains a single source module, and a defaults file that is opened, updated, and saved each time the program is run.

Six of the ARC codes were described in detail by Wintersteiner et al [*1996*]. The other two, RADV and OH_MODEL, are discussed in Section 2 of this report.

## A.2 SABER

The SABER directory contains two codes that we have used to process SABER Level 1B data. Both codes are works in progress, but have been used successfully in recent evaluations of SABER data. A complete description of each code will be prepared at such time as the code development is complete.

Briefly, the purpose of READ_SDAT is to enable researchers to access and process dozens or hundreds of L1B radiance data files, each corresponding to a single SABER "event". The purpose is to perform various tasks such as averaging, calculating statistics,

sorting according to various criteria, and writing specific quantities or profiles to output files for further consideration (e.g., plotting or analysis). The criteria currently in place for sorting include the latitude of the event, the local time, the solar zenith angle, and the tangent height (or range of tangent heights) of interest, and this can be done for one or several of the 10 radiance channels. There is also a tentative indicator for the strength of auroral activity seen by the channel-7 detector that can be used for sorting.

RAD_DIST is a code that performs two specific tasks using, as input, a particular type of file written by READ_SDAT. One purpose is to sort events according to the radiance levels at particular tangent heights, and to create output files giving the distribution of these levels (e.g., the number of events with radiance levels within each bin). Another is to generate the auroral indicator mentioned above.

Each of the subdirectories contains two files with source code. In each case, one file contains the main program and the other contains all the remaining source modules that are needed. In addition, each program has an associated directives file. Samples of these can be found in each subdirectory. These directives files have the names SDAT_NAMES and DIST_NAMES, and they each supply specific information needed to run their codes.

Very specific details about the tasks performed by each of these codes, the requirements for performing them, and the quantities to be read from the directives files are given at the beginning of the main source modules.